MULTIPLE SCATTERER RETRACKING AND INTERFEROMETRIC SWATH PROCESSING OF CRYOSAT-2 DATA FOR ICE SHEET ELEVATION CHANGES

SWADHIN NANDA

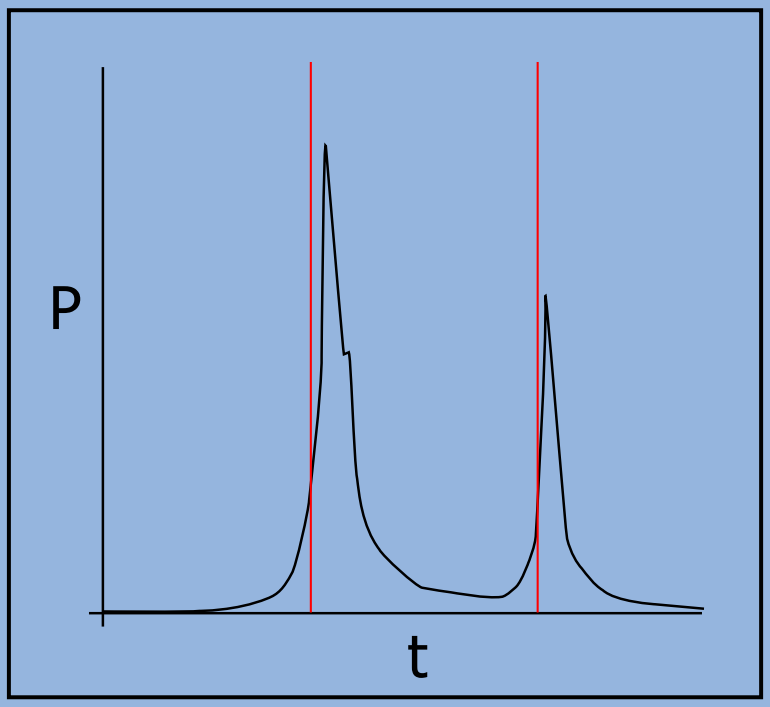

A study to fully utilise the CryoSat-2 data

Master of Science (MSc.)
Geoscience and Remote Sensing
Civil Engineering and Geosciences
TU Delft

July 2015

Multiple Scatterer Retracking and Interferometric Swath Processing of CryoSat-2 Data for Ice Sheet Elevation Changes,
A study to fully utilise the CryoSat-2 data
Master of Science (MSc.)
Delft, July 2015

Cover Illustration: A theoretical CryoSat SARIn received waveform with multiple peaks and the retracked positions on their leading edges

COMMITTEE:
Roland Klees
Miren Vizcaino
Cornelis Slobbe
Marcel Kleinherenbrink

ABSTRACT

In the processing of data acquired by conventional radar altimeters, algorithms designed to compute elevation of signal backscatterers assume that the point closest to the satellite antenna is the nadir point. While this is a valid assumption over the oceans, it is often not valid in non-oceanic surfaces. Radar altimetry data acquired over ice sheets, for instance, are dominated by multiple scatterers off-nadir to the satellite, which implies that more than one scattering surfaces in the radar footprint contribute to the received signal. A SAR/Interferometric Radar Altimeter, which is the primary payload of CryoSat, allows the geolocation of an off-nadir scatterer by recording the receiving signal in two distinct receiving antennae separated by a baseline of 1.2 m. In recent studies on ice sheet elevation changes based on CryoSat data, however, only one scatterer is 'tracked'. Hence, the full potential of the backscattered signal is not exploited. In this study, we design an algorithm that enables elevation estimation and geolocation of multiple off-nadir scatterers within the radar footprint from CryoSat Level 1b waveforms. With the results obtained by our CryoSat level 2 data processor, we obtain elevation change measurements over a part of the Jakobshavn Isbræ (or the Jakobshavn drainage basin) at West-Greenland. Our algorithm provides about twice as much retracked elevations compared to the number of elevations from the CryoSat ESA level 2 products, and hence a better spatial sampling of the elevation change signal.

ACKNOWLEDGEMENTS

This thesis takes a new step into ice-sheet monitoring using space-borne radar altimeters. In comparison to conventional altimetry techniques, the method described in this document not only provides a clearer picture of ice sheet exteriors, but also provides a means towards a better understanding of the dynamics occurring in the coastal ice sheet regions. I am excited to see how far radar altimeters can go, now that international scientific communities have embraced newer technologies, and are collaborating towards launching innovative radar altimetry missions. I hope that, in the context of ice-sheet monitoring, this thesis provides the reader with the means to take that first step into new-generation radar altimetry.

This document is the culmination of one year's research work conducted at the Department of Geoscience and Remote Sensing, in the faculty of Civil Engineering and Geosciences. If there is one lesson that I can take from working on this project, it is that research is the summation of dedicated, motivated hard work, and a lot of mistakes. Under the guidance of Cornelis Slobbe and Marcel Kleinherenbrink, I have had the opportunity to learn that mistakes are always necessary to produce good work. For that, they have my deepest gratitude; this project would not have been possible without their guidance on working with radar altimetry data and writing thesis reports. I am thankful to the staff of the GRS department, who never hesitated to provide me with insight, resources and the well wishes that played a key role in the timely completion of this project. I am extremely indebted to Pedro Inácio, who helped me with the supercomputer cluster, and gave me his valuable time to solve my command line problems.

I am especially thankful to Bert Wouters, who took time out of his busy schedule to read and reply to my endless queries about his latest work with the CryoSat mission. His insight and advice played a very important role in studying elevation changes with the results of the method designed in this thesis.I am thankful to V. Helm, A. Humbert and H. Miller from the Alfred Wegener Institute (AWI) for their contribution to elevation and elevation change estimate from CryoSat-2 data. I cannot forget to mention Lars Stenseng from DTU Space, whose PhD thesis on Polar remote sensing using CryoSat type altimeters played a significant role in understanding the different retrackers that have been implemented in this thesis.

I would like to thank my friends at TU Delft for providing the most important aspect of conducting research - taking that occasional coffee break and talking about anything but your work. I cannot forget

to mention my floor-mates at Delft, who provided insight into working on an MSc project. Lastly, I would like to thank my family and friends, without whose support (and the occasional counterproductive chit-chat) this thesis would not have been possible.

CONTENTS

LIST OF FIGURES

LIST OF TABLES

ACRONYMS

DORIS Doppler Orbitography and Radiopositioning Integration by Satellite

ESA European Space Agency

GLAS Geoscience Laser Altimeter System

GrIS Greenland Ice Sheet

GSFC Goddard Space Flight Center

ICESat Ice, Cloud and Elevation Satellite

LRM Low Resolution Mode

NASA National Aeronautics and Space Administration

NSIDC National Snow and Ice Data Center

OCOG Offset Center of Gravity

POCA Point of Closest Approach

SAR Synthetic Aperture Radar

SARInM Synthetic Aperture Radar Interferometric Mode

SARM Synthetic Aperture Radar Mode

SIRAL SAR Interferometer Radar Atimeter

WGS 84 World Geodetic System 1984

1

INTRODUCTION

The year 2014 (an El-Nino neutral year) is found to be the warmest year in the instrumental record (Cole, 2015) (since 1880). The Earth has warmed by 0.8 degrees Celsius since the first year of the instrumental record, which has caused accelerated melting of our planet's ice sheets. With such cause-and-effect running in motion, it is necessary to understand how climate change dynamics affect the Cryosphere of our planet. Ice sheets have proven to be an important area of study to analyse the consequences of Anthropogenic Global Warming and to forecast their contribution to the future climate change scenario.

The large scale hydrological activity ongoing in ice sheets is a fundamental starting point in their study. Inland precipitation causes the accumulation of snow, which gets compacted due to its weight and forms a denser ice base. The residual accumulated ice flows from the inland to the coast through gravity and exits the ice sheet as glacial flow. This cycle is maintained via inland re-precipitation, which is recharged by evaporation from the ocean. These set of natural phenomena maintain a balance between the incoming precipitation and outgoing runoff via marine terminating glacial flow. With warming of our Earth, there is a feedback mechanism that causes increased inland precipitation and glacial flow, and increased coastal losses. In fact, a net contribution of 19 to 30 millimeters to the Sea Level Rise (SLR) from four dominant marine terminating glaciers of Greenland has been forecast by the year 2200 (Nick *et al.*, 2013). In particular the Greenland Ice Sheet (GrIS) is an interesting area for monitoring ice melting because accelerated melting of the GrIS not only causes sea level rise but also weakens the Meridional Overturning Circulation (MOC). This has much more widespread consequences to regional and global climates (Hua *et al.*, 2011). The GrIS thinning can have potentially disastrous implications for settlements situated in the coastal regions. Hence, a system for continuous and accurate monitoring of ice sheets with a high spatio-temporal sampling needs to be realised.

Among a variety of parameters like temperature, wind, flow velocity, albedo, etc., probably the most important parameter necessary to understand the dynamics of ice sheets is topography (Remy & Parouty, 2009). Without the information of topography of the entire ice sheet, physical ice flow models, for instance, cannot be constrained. The topography of the exterior of ice sheets is quite variable. This poses the challenge; to be able to obtain elevation profiles over the entire ice sheet continent with a significant spatial sampling rate. Also, data acquisition should not be hindered by the presence

of clouds, which are quite common over ice sheets. Because satellite radar altimeters are unaffected by the presence of clouds, radar altimetry is a very robust technique to monitor ice sheets. Conventional satellite radar altimeters are pulse limited, such as ERS 1 launched in July 1991, ERS 2 launched in April 1995, and Envisat in March 2002. From the SeaSat mission in 1978, the GeoSat mission (1985-1990), to the Envisat mission (2002 - 2012), pulse limited altimeters have provided ice sheet elevation profiles, which have contributed to our understanding of ice sheet dynamics. For instance, the ERS mission helped determine a thinning of coastal Greenland by -2.0±0.9 cm/year and a thickening of the inland by 6.4 ± 0.2 cm/year, over a period from 1992-2003 (Johannessen *et al.*, 2005). Another excellent example of the resourcefulness of satellite radar altimetry is the mapping of active subglacial lakes by McMillan *et al.* (2013).

The concept of altimetry is quite simple - the satellite sends a signal which bounces off a surface scatterer within the satellite footprint and is received at the satellite. This received signal is recorded and from it the two way travel time is derived, which is used to obtain the range information of scatterer to the satellite. With the orbital information of the satellite, the position and elevation of the scatterer are estimated. However, conventional altimetry provides the user with data with a low spatial resolution since instruments generally have a beam footprint in the order of 10-20 km. The elevation that is computed from the two way travel time of the signal is conventionally assigned to the nadir point, as there is no way of locating the actual position of the scatterer within the footprint. With such coarse measurements it is unreliable to compute elevation changes as the user might be computing elevation changes between two different scatterers lying within the same footprint in two distinct satellite passes. This, in particular, occurs over coastal regions of ice sheets, where the topography is very variable. Raney (1998) presented a novel radar altimeter concept that resulted in more accurate data with a higher along-track resolution. The so called delay/Doppler altimeter utilises the multi-looking concept of side-looking Synthetic Aperture Radars. Due to this 'multi-looking' and coherent averaging of 'bursts' of Radar backscattering pulses according to their Doppler frequency, the variance of elevation estimates is reduced. This kind of altimetry was first realised in the CryoSat mission's Synthetic Aperture Radar Interferometric Altimeter (SIRAL) instrument, which has a beam footprint of 15 km in the across track direction and 300 m in the along track direction in two of its three modes.

The general ice sheet topography is marred with crests, troughs, rough terrain in the ice sheet exteriors, and sloping terrain. This causes a large ambiguities while using conventional altimetry for computing elevation of surface scatterers over ice sheets. This is because the primary assumption made in conventional altimetry is that

the point-of-closest-approach to the satellite (POCA) is the nadir point. Because of this, the computed elevation is assigned to an incorrect point on the ellipsoid. To solve this problem, a phase monopulse altimetry technique was proposed by Jensen (1995) that utilised two different antenna to receive the backscattered signal. The phase difference between the two antennae provided the direction of the scatterer with respect to the antenna's pointing direction (or boresight). This contribution was the first one that did not need an additional reference DEM to resolve the effects of cross track slope in the received waveform. It was a significant breakthrough that led to the development of the CryoSat mission.

The launch of CryoSat-2 in 2010 has marked the beginning of an entirely new type of satellite radar altimetry (Wingham *et al.*, 2006). With an orbital inclination of 92 degrees, the CryoSat mission provides near global coverage with a large track density in the higher latitudes. The CryoSat mission is the first satellite mission to be equipped with a delay-doppler altimeter along with a secondary receive antenna to provide interferometric measurements that allows the determination of receive angles of the scattered waveforms. This satellite altimetry mission is equipped with three altimeter modes - the Low-Resolution mode (LRM), the Synthetic Aperture RADAR mode (SARM) and the Synthetic Aperture Radar Interferometric mode (SARInM). The principal innovation in the CryoSat mission is the SAR/Interferometric Radar Altimeter (SIRAL), that combines a delay/Doppler SAR altimeter with phase monopulse interferometry. With these technologies, the SIRAL instrument is able to provide information about the position and elevation of the scatterer in the SAR footprint.

The conventional radar altimeter paradigm is to obtain one elevation measurement per received waveform. While this has been the prevalent practice, with the advent of CryoSat, it is now possible to geolocate multiple scatterers. This project documents a novel technique in elevation retrieval of scattering surfaces which utilises the full capabilities of the SARIn mode of the SIRAL system of the CryoSat mission. The following sections will discuss the research work leading to the inception of this project, the research objectives and questions driving this research.

1.1 A HISTORY OF SATELLITE RADAR ALTIMETRY AND RETRACKING ALGORITHMS FOR ICE SHEET MONITORING

The very short 106-days mission of the SeaSat-1 satellite in 1978 provided valuable satellite altimetry data over continental ice sheets. A radar return pulse waveform is a record of the returned pulse power with respect to the time of receive. The SeaSat-1 altimeter was designed to record the shape of the leading edge of the return pulse waveform. This objective was partly achieved by utilising a low band

pass filter, dubbed as the alpha-beta tracker, that maintained the leading edge of the return pulse waveform. While this was accomplished over ocean surfaces and ice sheets with a topographical slope of less than 1°, the tracker failed to locate the leading edge of the return pulse at the center of the waveform from areas of high topographical variability. This lead to a departure of the leading edge of the received waveform and the tracker position in the return waveform. Martin *et al.* (1983) developed a set of routines that located this departure from the tracking bin. This method was known as 'retracking', which re-located the position of the leading edge of the return pulse with respect to the position of the tracking bin. They showed that retracking radar waveforms that were generated from received backscattered signal could improve SeaSat-1 satellite range measurements over ice sheets by 10 m (Martin *et al.*, 1983). The concept of leading edges and radar waveforms are discussed in Chapter 2 and Chapter 3.

One of the interesting observations that Martin *et al.* (1983) made in their study was the existence of multiple 'ramps' in the received power, which was identified as off-nadir pulse interactions. A *ramp* or a *peak* in the received pulse waveform corresponded to an increase in the returned power due to the receiving of backscattered signal from a surface scatterer lying in the radar footprint. The fact that they observed more than one *peak* was indicative of multiple scatterers in the radar footprint. Although their algorithm did not geolocate these multiple peaks, it was the first approach that took this phenomenon into account and retracked multiple scatterers. Their retracking algorithm was adopted by NASA's Ice Altimetry Group as the NASA GSFC V4 algorithm.

Martin *et al.* (1983) pointed out that return waveforms over ice sheets were not spatially consistent and were dominated by errors due to, (i) sloping surfaces, (ii) off-nadir reflections, (iii) undulating surfaces with variations in similar spatial scales as the radar footprint, and (iv) dynamic lag of altimeter tracking circuit, primarily due to variable topography. In elevation change studies, it is critical to correct for such sources of error, and geolocate the scatterers as accurately as possible to avoid incorrect elevation change estimates (dH/dt) (Hurkmans *et al.*, 2012a). In particular, sloping surfaces are a primary cause of errors in elevation estimates as the POCA is upslope and not at the nadir point, and the elevation corresponding to it is assigned to the nadir point. To tackle this problem, three popular techniques were designed (Bamber, 1994), (i) The 'Direct technique' designed by A.C. Brenner (1983), (ii) The 'Relocation method' designed by A.C. Brenner (1983), and (iii) The 'Intermediate technique' designed by F. Remy & Minister (1989). In summary, the direct method applies no correction to the position, the intermediate method applies no correction to the range but to the position. The relocation method applies a correction to both range and position

(Bamber, 1994). All three methods used *a-priori* information of the slope via a reference DEM, and hence the quality of their results was dependent on the quality of the DEM. Note that this is resolved with the phase monopulse approach by Jensen (1995), which does not rely on an external apriori source of information.

Radar return waveforms are usually noisy, which significantly affect the fit of an analytical model through the received waveform. With the launch of ERS-1 and ERS-2, ESA's primary algorithm developed was the Offset Center Of Gravity (OCOG) algorithm (Wingham *et al.*, 1986). This was the first retracking algorithm that did not fit an analytical model through the received data, and hence was a more robust approach in processing received radar waveforms. It located the leading edge of the waveform by offsetting the position of the center of gravity of the received waveform. This method is discussed in Chapter 3 and is one of the methods implemented in this study.

One of the critical factors that need to considered in using radar signals over ice sheets is its penetration into the ice. A Ku-band (wavelength of 2.3 cm) radar signal can penetrate several meters into the ice, causing multiple reflections from the surface of the ice and the subsurface layering. Such a 'multipath' effect results in both surface and volumetric backscattering and was first observed by Ridley & Partington (1988). There was a need to design a retracking method that took into account this ability of radar signals. Davis (1993) developed the first re-tracking algorithm that took into account the penetration of radar signal into the ice, for ice sheet satellite radar altimetry. This algorithm employed a non-linear combined surface and volume scattering model that was fit through the waveform using an iterative least-squares approach. However, fitting a model through noisy received waveforms can result in incorrect results.

Davis marked a need for consistent techniques that ensured a *repeatable* retracking point in the waveform to reduce the likelihood of errors and biases appearing in the computed elevation. He introduced a new empirical algorithm known as the threshold retracking algorithm that provided more repeatable results when compared to the OCOG and V4 algorithms (Davis, 1997). The threshold algorithm is similar to the OCOG algorithm in the sense that both of them do not employ an analytical model into their leading edge computation. However, the threshold retracking algorithm was superior, in the sense that it provided the user with the control to choose the kind of threshold at which waveforms could be retracked in a consistent manner. This new algorithm was adopted by NASA over the GSFC V4 algorithm. Due to the flexibility and robustness of the threshold retracker, it is commonly used to retrack waveforms over ice sheets for elevation change studies (Brenner *et al.*, 2007).

All satellite radar altimeters launched before CryoSat were not equipped with a dual receiving system that made it impossible to correct for

slopes without apriori information of the topography within the radar footprint. The SIRAL altimeter enables the geolocation of off-nadir scatterers on sloping terrain, at a higher spatial resolution, without the use of an apriori information source. This feature is the primary technology that makes the CryoSat mission a reliable remote sensing system to monitor ice sheets. Currently, it is the only satellite mission that is designed to monitor polar regions since the loss of the ICESat mission in 2009 and the ENVISAT mission in 2012. McMillan *et al.* (2013) demonstrated the ability of the CryoSat mission to monitor subglacial lake volume changes. They combined data from the ICESat mission and the CryoSat mission to monitor the surface depression of Antarctic subglacial Lake Cook_{E2}, which was reported to lose between 2.9-6.4 km^3 of water during a flood event between 2007-2008. This observation was made possible due to the SARIn mode of the SIRAL instrument, which enabled McMillan *et al.* (2013) to observe the progression of the flood event with detailed 3-D mapping.

One of the most significant contributions towards ice sheet monitoring with CryoSat was that of Helm *et al.* (2014), who created a DEM with their novel Threshold First Maximum Retracking Algorithm (TMFRA). From their algorithm, they provided elevation change information between 2011 to 2014 over Greenland and Antarctica, and over the Jakobshavn Isbræin the south-west coast of Greenland (Helm *et al.*, 2014). Their study demonstrated the important role the CryoSat mission played in observing the polar regions of the Earth. With the support of processing techniques developed by Helm *et al.* (2014), Wouters *et al.* (2015) provided direct evidence of glacial thinning in the Southern Antarctic Peninsula.

The contribution on CryoSat that drives the motivation of this study was provided by Gray *et al.* (2013), who explored the possibility of utilizing data in the return waveform that corresponded to scatterers beyond the POCA within the radar footprint. They reported a swath processing method that resulted in height measurement beyond the POCA for an average cross track slope between $0.5° - 2°$. Their results increased the data volume by an order of 2 magnitude (Gray *et al.*, 2013). This result motivates this study, in which we attempt to retrack scatterers beyond the POCA.

1.2 RESEARCH OBJECTIVE AND RESEARCH QUESTIONS

This study aims to fully utilize CryoSat data to extract information about multiple scatterers within the radar footprint over ice sheets exteriors. In doing so, it is needed to come up with a technique or a modification that looks at the entire received waveform, identifies possible *peaks* in the waveform that may represent multiple distinct scatterers in the radar footprint, and retracks them separately to obtain the information of satellite range to these different scatterers. For

this, the SARIn mode needs to be incorporated so that these distinct scatterers are located at different positions along the swath of the satellite. It is expected that a successful development of such a procedure may increase the amount of data points within the region of interest. To study the impact of such an algorithm, elevation change studies are conducted, and the results are compared with the outcome of the CryoSat Level 2 Processor developed by the European Space Agency. So, our primary research objective is,

To Design an algorithm that utilizes the entire return echo data of CryoSat to study ice sheet elevation changes.

From this objective, three research questions are proposed.

1. *Can a retracker process CryoSat SARIn waveforms to retrieve multiple elevation estimates per waveform?*

   This question drives the designing phase of the project. To retrack SARIn waveform peaks from multiple scatterers, we will design a subwaveform retracker modification, that will be implemented over existing retrackers. This subwaveform retracker is coupled to a brute force interferometric processing algorithm that takes into account ambiguities in phase due to surface topography.

2. *How does the proposed retracking scheme compare to the available Level 2 CryoSat SARIn data products from ESA?*

   To assess the impact of the proposed method, we will compare our results to those from the CryoSat ESA Level 2 products over the same region of interest. Our selected region of interest in the Jakobshavn Isbræ, which lies on the south-west coast of the Greenland ice sheet.

3. *What is the impact of applying this developed technique in studying ice sheet elevation changes?*

   To compute elevation changes over the period that the baseline B data are available (July 2010 to March 2015) over the Jakobshavn Isbræ we adopt the method developed by Wouters *et al.* (2015). For assessing the performance of the designed retrackers, we choose the Jakobshavn Isbræ as our region of interest because:

   i) CryoSat SARIn data from 2010 to 2015 is quite large and vastly increases the computation time in comparison to choosing a smaller area like the Jakobshavn Isbræ instead of the entire coastal zone of Greenland.

   ii) Jakobshavn Isbræ experiences a large magnitude of losses that have been scientifically well documented and observed with the help of remote sensing systems like an airborne

and space-borne lidar, satellite gravity missions, radar altimetry, etc.

We also compute elevation changes from CryoSat level 2 data using the same method, and compare them with our results.

1.3 OUTLINE

In Chapter 2, we discuss the innovations of the SIRAL altimeter and explain how the received waveforms look like. We introduce some example waveforms that were recorded over ice sheets.

In Chapter 3, we discuss the concept of retracking. The different retrackers used in this study are introduced, and the developed subwaveform retracker modification is discussed. After that, we introduce the interferometric processing and geolocation algorithm that was implemented along with the designed retracking approach. We include the entire flow diagram of the routines implemented in this study.

In Chapter 4, we discuss the results of these retrackers and compare them to the Level 2 CryoSat data products from ESA.

In Chapter 5, we conclude by answering the research questions and the research objectives and provide recommendations for future research.

2

CRYOSAT: THE MISSION, ITS MODES AND ITS PRODUCTS

Satellite radar altimetry is the remote sensing technique to measure the range of the surface to the satellite using by measuring the time taken for a microwave signal to travel from the satellite to the surface and back. This two-way travel time is necessary to compute the elevations of surfaces with respect to the WGS 84 ellipsoid. The latter requires precise time-keeping along with a very specific knowledge of the satellite's orbital position and altitude with respect to a specific reference ellipsoid. The orbital information is obtained with the help of orbit determination systems like DORIS, which uses a network of 50 ground beacons over the entire world. These beacons transmit signals to a satellite's *Doris receiving antenna* and utilise the Doppler shift of signals to provide very precise orbital position.

The pulses emitted by these altimeters illuminate a nearly circular area on a flat surface, known as the footprint of the altimeter. The *beam-limited* footprint of a satellite radar altimeter is described by the following equation,

$$D = 2h \tan(\theta/2), \tag{1}$$

where D is the footprint diameter, h is the altitude of the satellite with respect to the ellipsoid, and θ is the 3 dB beamwidth of the antenna. The *beam-limited* footprint of a satellite radar altimeter at a height of 717 km and with a 3 dB beamwidth of approximately 1.2 degrees is around 15 km. The footprint of a satellite radar altimeter determines the spatial resolution of the data; the larger the footprint, the lower the spatial resolution. Hence, radar altimeter footprints of 15 km do not provide sufficient resolution to monitor topography, like ice sheets, which have a high topographical variability within the footprint, even though such a footprint can provide sufficient resolution to monitor a relatively invariant topography, like the ocean surface. In monitoring the entire globe, the SIRAL altimeter onboard the CryoSat mission is the first of its kind that utilises a multi-mode approach to provide sufficient spatial resolution over areas with topographical variations in the sub-kilometer scale.

This chapter provides an overview of the CryoSat mission, describes the SIRAL altimeter in comparison to conventional altimeters, and gives examples of its data over ice sheets.

2.1 THE CRYOSAT MISSION: A BRIEF LOOK ON THE TECHNICAL DETAILS

The CryoSat-2 mission (Figure 1), hereafter just referred to as CryoSat, was launched on April 8, 2010, for an intended mission life of three years and eight months. The satellite has a non sun-synchronous low Earth orbit at an approximate altitude of 717 km above the WGS84 ellipsoid, an inclination angle of 92°, and a repeat orbit of 369 days with a 30-day sub-cycle. The goals of the mission are: i) recovering regional and basin-scale trends in Arctic sea ice thickness and total mass, and ii) estimating the contribution of shrinking of Antarctic and Greenland ice sheets to the global sea level. The secondary goals of the mission are: i) observation of the seasonal and interannual variability of Arctic and Antarctic sea ice thickness and mass, and ii) observation of variations in thickness of ice caps and glaciers (Wingham, 1999). These goals are facilitated by:

1. An orbital inclination of 92°, which provides coverage of up to ±88° latitude. This inclination angle is particularly beneficial to monitor Greenland and Antarctica, as the orbital inclination facilitates a much denser network of satellite tracks at higher latitudes.

2. The onboard state-of-the-art altimeter (SIRAL), which operates incorporates delay/Doppler altimetry and phase monopulse interferometry over coastal regions of ice sheets with a footprint size of 0.3 km in the along-track direction and 15 km in the across-track direction (Wingham *et al.*, 2006). This altimeter provides data with a higher spatial resolution in the along-track direction, which is an important feature to monitor ice sheets.

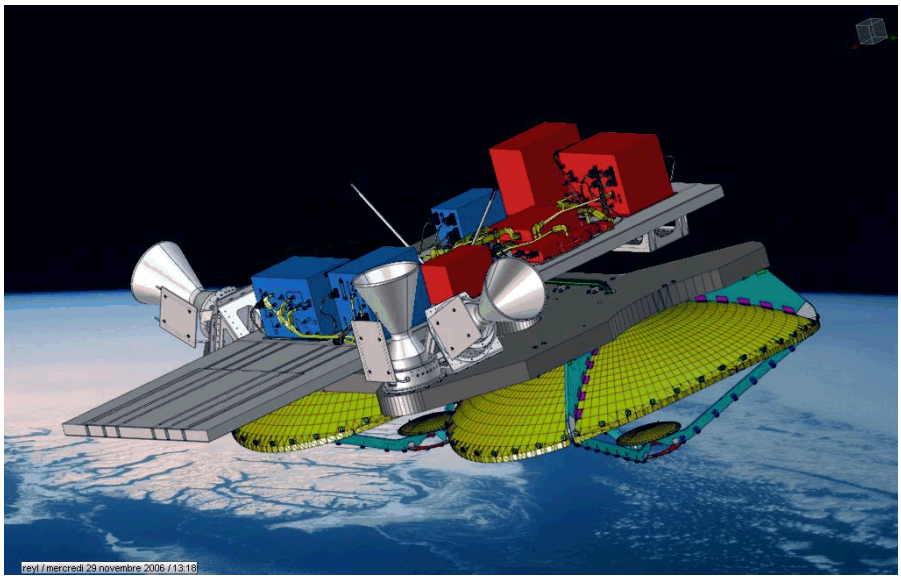

Figure 1: A picture of the CryoSat-2 satellite. The most pronounced feature of the CryoSat satellite is its two SIRAL antenna. Image obtained from www.esa.int.

2.1.1 *The SIRAL instrument: A brief insight into the altimeter modes*

SIRAL, or SAR/Interferometric Radar Altimeter, is the principal instrument onboard the CryoSat satellite. It has three modes of operation. The mode of operation depends on the area above which the satellite flies. The three modes of operation are: (i) the Low Resolution Mode (LRM), (ii) the Synthetic Aperture Radar Mode (SARM), and (iii) the Synthetic Aperture Radar Interferometric Mode (SARInM). Table 1 provides all relevant parameters of the SIRAL instrument. A map of the CryoSat mode mask is provided in Figure 2.

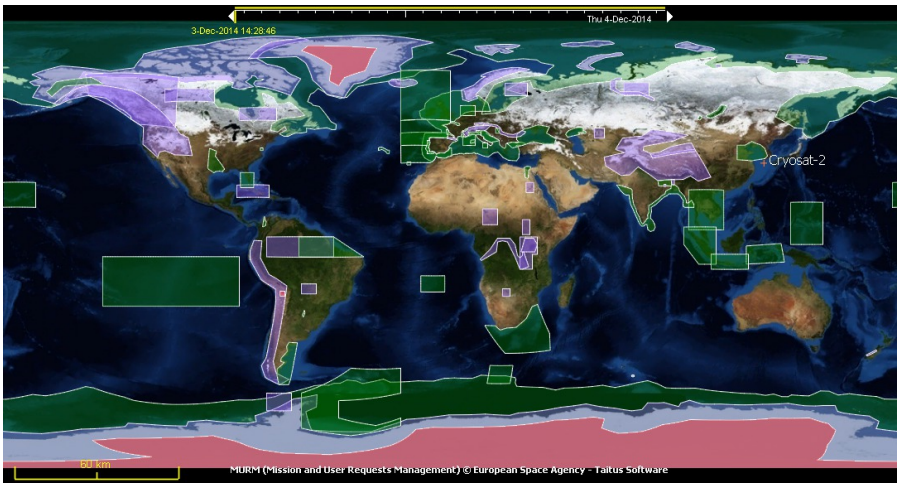

Figure 2: This Geographical mode mask of CryoSat for 2014 over the entire world shows the regions of SAR mode (green), the SARIn mode (purple) and the LRM mode (red) acquisitions. Image obtained from ESA.

2.1.1.1 *Low Resolution Mode*

The LRM is the conventional altimetry mode of the satellite and results in an approximate footprint size of 15 km. This wide footprint is sufficient over open oceans and the interior of ice sheets where the topography is usually smooth. The LRM mode utilises a single antenna, and transmits a 13.575 GHz signal with a 350 MHz bandwidth at a Pulse Repetition Frequency (PRF) of 1.971 kHz, which corresponds to a Pulse Repetition Time of 507 µs. The length of the pulse is 49 µs. This means that at a height of 717 km, the instrument in the LRM transmits a pulse that is received approximately 4.78 ms later. Only 44.8 µs of the return echo is recorded, which reduces the receiver bandwidth to 320 MHz. The processed LRM data covers a range window of 60 m for each return echo, sampled over 128 bins with a bin width of approximately 0.47 m. Because the LRM has a very large footprint, it is not suitable for the coastal margins of the ice sheets and sea ice measurements.

Table 1: The parameters are: i) f frequency in GHz, ii) $B_{receive}$ the received bandwidth in MHz, iii) PRF, the pulse repetition frequency in kHz, iv) t_{pulse} is the pulse duration in μs, v) N_{bins} is the number of bins in the waveform, vi) 3 dB Angle is the look angle in degrees (along track x across track), vii) d is the footprint size (along track, across track), and vii) $\triangle_{rb}$ is the length of the range bin sample (in meters).

	LRM	SARM	SARInM
f (GHz)	13.575	13.575	13.575
$B_{receive}$ (MHz)	320	320	320
PRF (kHz)	1.97	18.181	18.181
t_{pulse} (μs)	44.8	44.8	44.8 s
N_{bins}	128	128	512
3 dB Angle (in degrees)	1.0766 x 1.2016	1.0766 x 1.2016	1.0766 x 1.2016
d (km)	15	0.3	0.3
		15	15
$\triangle_{rb}$ (m)	0.4686	0.2342	0.2342

2.1.1.2 *Synthetic Aperture Radar Mode*

The SAR mode employs *delay/Doppler* or *SAR* altimetry developed by Raney (1998). In this mode, 64 pulses are transmitted in bursts at a PRF of 18.181 kHz and a Burst Repetition Frequency (BRF) of approximately 87.5 Hz. At a height of 717 km, these bursts are received 4.78 ms later. These received echoes from a single burst are processed at the processing facility, where single-look waveforms are generated for received pulses from 300 m strips in the along-track direction. These single look waveforms are combined to create a multi-looked waveform for that 300 m strip.

The along-track footprint width $\triangle x$ in *delay/Doppler* or SAR altimetry can be calculated using the,

$$\triangle x = \frac{1}{N_B} \frac{h\lambda}{2V_{S/C}T_{PRF}}, \tag{2}$$

where λ represents the pulse wavelength, $V_{S/C}$ represents the velocity of the satellite along its orbit, T_{PRF} represents the pulse period and N_B represents the number of pulses per burst. Using values provided in Table 1, we arrive at an along-track footprint width of approximately 300 *m*. This unique footprint characteristic is particularly useful to monitor sea ice and the exterior of ice sheets. Figure 4 provides a graphical representation of the footprints involved in the SIRAL instrument. It is important to note that before the signals corresponding to that specific strip are combined, they are zero-padded to

decrease the waveform bin size to 1.5625 ns or 0.23 m (in the current release of CryoSat data products (Baseline B), the SARM waveforms are cut to 128 bins, covering a range window of 30 m). The resulting waveform has different characteristics in comparison to LRM waveforms and is discussed in the following section.

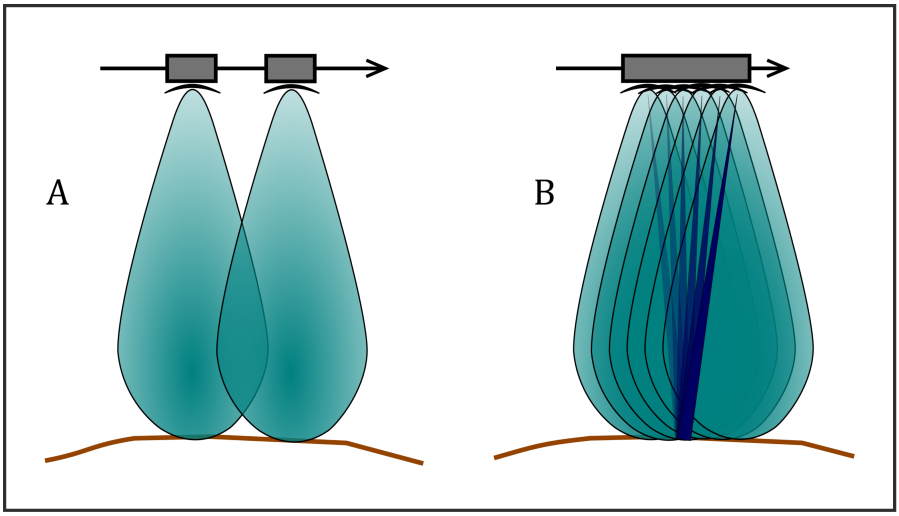

Figure 3: *A.* The figure represents conventional altimetry over a scattering surface. The pulse, which is represented in green, represents the entire area in the footprint. *B.*

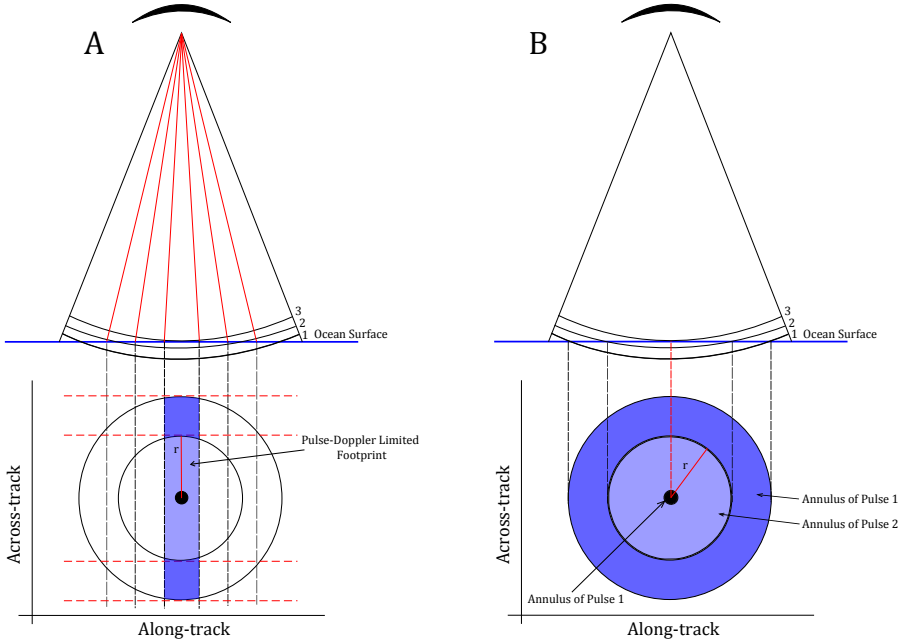

Figure 4: CryoSat footprints in SARM/SARInM (footprint *A*) and LRM (footprint *B*). Figure adopted from Scagliola (2013).

2.2 THE CRYOSAT SYNTHETIC APERTURE RADAR INTERFEROMETRIC MODE

An innovation in the SIRAL instrument is the Synthetic Aperture Radar Interferometric mode or the SARInM. This mode has the same footprint characteristics with the SARM and differs from LRM and SARM in the receiving chain — The SARInM uses two antennae the backscattered signal. This feature allows to compute cross-track angles at which signals arrive. The SARInM uses the burst mode and transmits 64 pulsed bursts at a PRF of 18.181 kHz (just like the SARM), but differs in the BRF, which is at about 21.4 Hz. After receiving the signals, they are sampled into 512 complex bins. This increases the range window to 120 m. This sampling is done to accommodate the larger topographical variations in the exterior of ice sheets. The SARInM is also equipped with an onboard tracker that determines the exact time at which the measurement window is opened by *pre-surveying* the ground surface. This onboard tracker has a much larger window of 480 m to capture the strong topographical variations in ice sheet exteriors. In some cases, the topographical variations are too large, and the onboard tracker fails. In such a situation the tracking window is opened either too early or too late. This causes the returned signal to fall partly or wholly outside the measurement window. It is important to keep this in mind while processing the data.

For surfaces with large topographical variations over short distances, a received SARIn waveform can sometimes have more than one *peaks*.

This is a common phenomenon in the exterior of the Greenland ice sheet. These *peaks* correspond to multiple scatterers in the illuminated surface. Also, depending on the type of surface the radar pulses can penetrate into the surface and cause a delay in their receive time. If the penetrated radar reflects back to the satellite and falls within the measurement window, it can appear as a *peak*. Because of this, it is important to study the reasons for such occurrences and identify which waveform peak corresponds to off-nadir scatterers and which waveform peaks correspond to pulse penetration into the surface. In our project, it is assumed that the reflections received are primarily due to off-nadir scattering surfaces. Figure 5 provides a graphical explanation of the generation of a received waveform over surfaces with large order topographical variations over within the radar footprint.

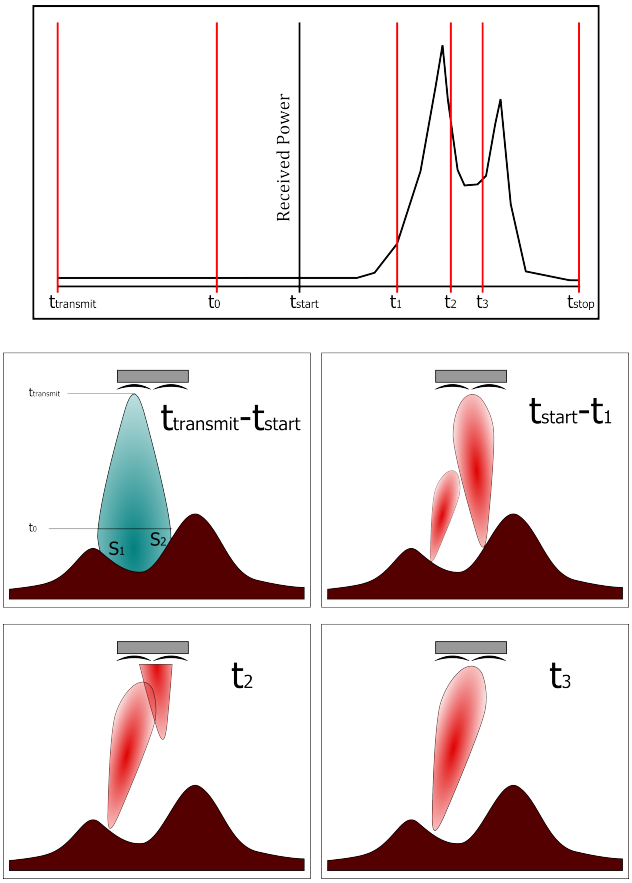

Figure 5: The waveform of the received signal from a surface in not recorded from the time of transmission of the signal $t_{transmit}$. Between the time of start of transmission and the start of receiving and recording the signal t_{start}, the pulse from the satellite altimeter first reflects off surface S_2 and then from surface S_1, as S_2 is closer to the altimeter than S_1. Because of this, the first signal recorded is from the surface S_2 at time t_1. At time t_2, the tail end of the pulse is recorded, which consist of weaker backscatter from S_2. Finally at t_3, the backscattered signal from S_1 reaches the altimeter and starts getting recorded. At t_{stop}, the measurement window terminates and beyond this no reflections are recorded. The figure is not drawn to scale and the lobes do not represent full backscatter behaviour.

A signal returning to the altimeter is received by both antennas. Depending on the position of the scatterer with respect to the position of the satellite, t signal received at one of the antenna may have travelled a longer distance than at the other antenna. If the receiving signals are in phase, it implies that the signals either have the same path length or the path difference of the signals is an integer multiple of the signal's wavelength. Also, if the antenna receive two similar amplitude signals at the same time from two distinct scatterers, a phase difference of zero is computed for that receiving time. If the same signal received by the two antenna comes from an off-nadir point, the received signals will not be in phase. If θ is the angle of the scatterer with respect to the normal from the satellite's CoM to the nadir, and B is the baseline of the antennas, the extra distance travelled $\triangle r$ by the return signal to one of the antennas is $B \sin\theta$ (see Figure 6). This extra path length causes a phase difference that is proportional to the fraction of the wavelength of the received signal: $\triangle\phi = \frac{2\pi B \sin\theta}{\lambda}$. Using the relationship between the path difference and the phase difference, the receiving angle of the signal is $\theta = \sin^{-1}\left(\frac{\triangle\phi\lambda}{2\pi B}\right)$.

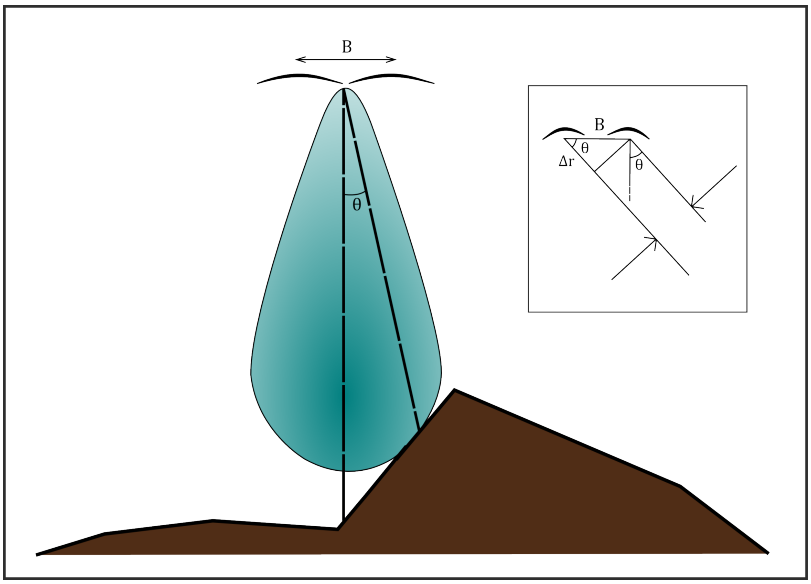

Figure 6: In the SARInM, CryoSat exceeds the performance of other altimeters over areas with strong topography, by being able to geo-locate off-nadir scattering surfaces. Here, the POCA is at an angle θ from the nadir point. With the accurate knowledge of CryoSat's baseline B, and the information from the on-board interferometer, it is possible to compute the receiving angle θ of the pulse. Implementing this approach in elevation computation results in geo-located positions of off-nadir scatterers.

2.2.1 *The CryoSat received waveforms*

Due to the unique characteristics of the SAR altimeter, its waveforms are much different from conventional pulse limited altimeter received waveforms. To illustrate the differences in waveform types between conventional altimeters and the *delay/Doppler* or SAR/SARIn altimeter, a graphical example of waveforms acquired over open oceans is shown in Figure 7.

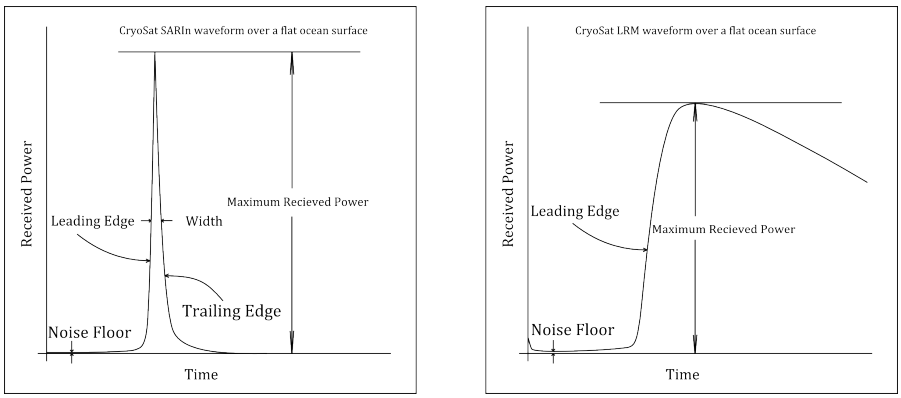

Figure 7: A typical CryoSat waveform over flat ocean surface with low roughness versus a typical pulse limited waveform. Here, the influence of along-track Doppler processing is clearly visible; the leading edge slope and the trailing edge slope are very abrupt in the SARIn waveform, as compared to the waveform in the LRM.

To understand the reason for the differences of waveforms generated by the SAR altimetry and conventional altimetry over the same surface, let us look at Figure 4 which represents two cases: Figure 4.A describes a SAR footprint and Figure 4.B represents a conventional altimeter footprint. The surface is a flat surface (in this case, an ocean). For the sake of simplicity, a pulse sampled at three different instances is shown. The pulse at position 3 has just reached the surface, and at positions 2 and 1, it has already interacted with the surface and is returning to the satellite. The blue colored rings represent the surface area illuminated by the pulse at different time intervals. The sharpness of SARM/SARInM waveforms arises from the differences in the illuminated area over time, as the amount of energy being backscattered to the satellite is proportional to the illumination area. In case of conventional altimetry, there is an increase in the illuminated area from pulse position 1 to 2, which decreases at pulse position 3. This results in a gradual trailing edge slope in the waveform. In case of SAR altimetry the illuminated area drastically increases and decreases with time, which corresponds to a sharper trailing edge in the received waveform.

2.2.1.1 *Examples of SARIn waveforms*

Some examples of SARIn waveforms over ice sheet topography are provided in this section, along with the ground track of the satellite and the nadir point of the satellite when the echo was recorded. A satellite image obtained from Landsat 8 is provided to show the type of terrain illuminated by the radar footprint. The date of LandSat 8 acquisition does not coincide with the date of CryoSat acquisition. The CryoSat acquisition was on 22-Aug-2014.

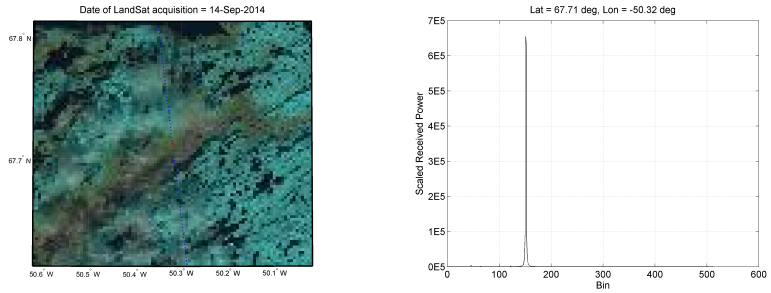

(a) LandsSat 8 Image (b) Single scatterer specular waveform

Figure 8: The waveform in this example corresponds to a single scattering surface in the radar footprint.

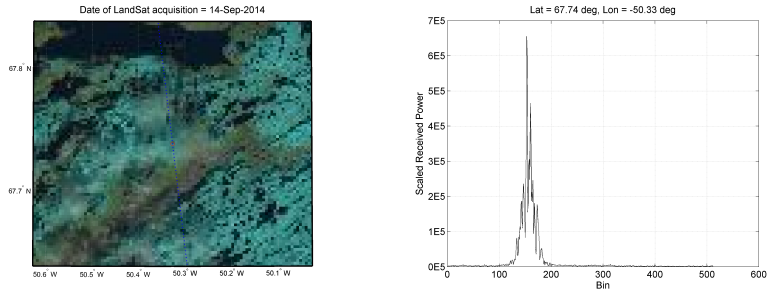

(a) LandsSat 8 Image (b) Waveform affected by noise

Figure 9: The waveform in this example is clearly affected by noise. Nevertheless, there seems to be a signal from a scattering surface.

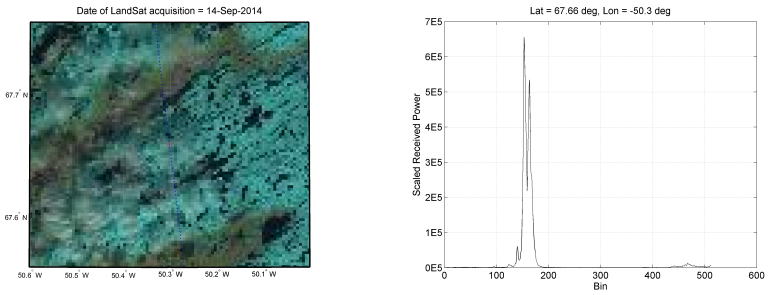

(a) LandsSat 8 Image

(b) SARIn waveform with multiple *peaks*

Figure 10: This is an exampe of a SARIn waveform with two distinct peaks. These peaks could represent two distinct scattering surfaces within the radar footprint. However, it is also possible that this waveform could be possible due to penetration of the transmitted signal into the ice. Without phase difference information, it is very difficult to know with certainty which is the case.

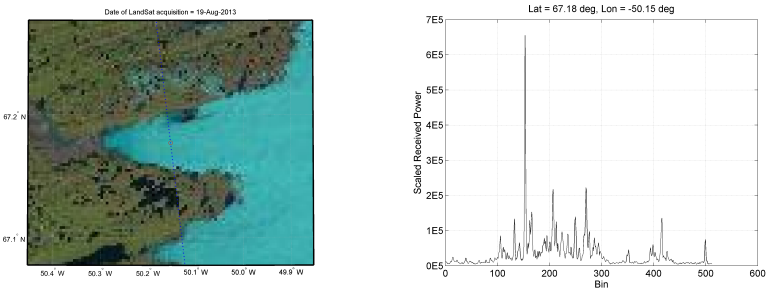

(a) LandsSat 8 Image

(b) A noisy waveform with a distinct scatterer at bin 150

Figure 11: Looking at the terrain from the LandSat 8 image, we may deduce that the noise in the waveform could be because of weaker backscattered signals due to radar pulse penetration. Because it is very difficult to conclude this with certainty, we implement a criterion in our study that filters out peaks with low return power.

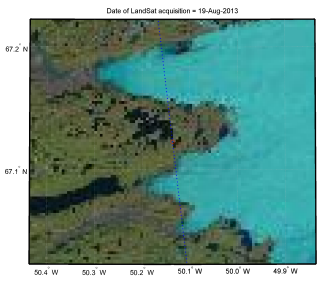

(a) LandsSat 8 Image

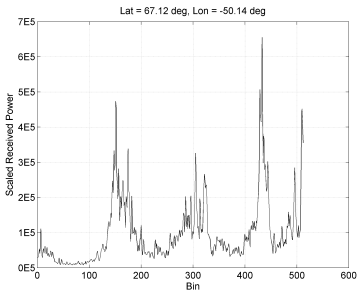

(b) A very noisy received waveform

Figure 12: This is an example of a very noisy return waveform over ice sheet topography.

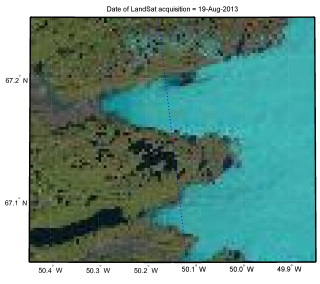

(a) LandsSat 8 Image

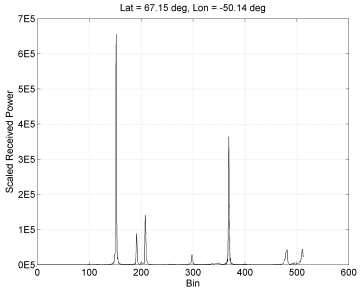

(b) SARIn waveform with multiple *peaks*

Figure 13: This is a clear example of a received SARIn waveform with multiple scatterers within the radar footprint.

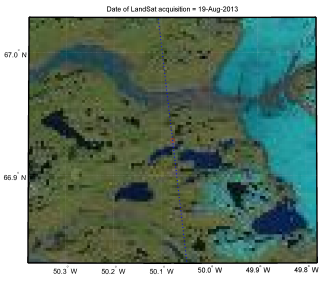

(a) LandsSat 8 Image

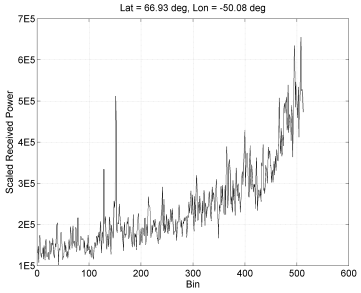

(b) Extremely noisy waveform

Figure 14: This is an example of an extremely noisy waveform. These waveforms are discarded in the data editing prior to the actual retracking. These kind of waveforms are primarily affected by incorrect *pre-estimation* of the expected range to the surface by the onboard tracker (see Section 2.2).

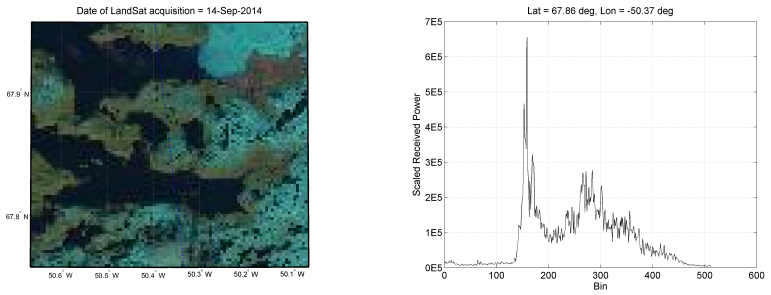

(a) LandsSat 8 Image (b) Noisy waveform

Figure 15: This could possibly be due to backscattering of the signal from many different types of scattering surfaces - ice, earth, or water.

2.3 SUMMARY

The CryoSat mission is currently the only dedicated mission that provides radar altimetry data over the polar regions of the Earth. The SARIn mode of the SIRAL altimeter provides higher spatial sampling. This feature is advantageous in monitoring elevation changes over the ice sheet exteriors where the spatial variability of the topography is quite high over distances in the order of 100 m. This chapter provided the properties of the the CryoSat SIRAL altimeter and its data.

The leading edge of these waveforms carries the necessary information about the exact arrival time of the backscattered radar pulse, and provides us with the two-way travel time of the radar pulse between the SIRAL altimeter and the scattering surface(s). By so-called retracking, the exact gate (or bin, or range sample) at which the pulse is received can be determined, from which elevation of the scattering surface(s) can be computed. In the next chapter, the concept of retracking is discussed in depth.

3

RESEARCH METHODOLOGY

The satellite tracker of a radar altimeter almost always has an idea about the two-way travel time of the transmitted radar signal, unless the onboard tracker fails (see Chapter 2, Section 2.2). In a CryoSat received waveform, the midpoint bin acts as the reference point of the received signal, which corresponds to the two-way time between the emitted pulse to the midpoint of the received waveform. This reference point does not always coincide with the leading edge of a peak in the radar waveform. The process in which the leading edge of the peak corresponding to a surface scatterer within the radar footprint is re-adjusted to improve range results is known as retracking.

Simply implementing a retracking algorithm is usually not enough for SARIn waveforms over ice-sheets. Because satellite altimeters are inherently nadir pointing, it is assumed that returns from a flat surface parallel to the orbital plane of the satellite originate from the nadir point of the satellite. When the topography is uneven and sloping, this assumption is incorrect, resulting in large errors in elevation estimates. Because of this, an algorithm to compute elevations from CryoSat altimetry measurements also needs to include an interferometric processing algorithm that takes advantage of the dual receiving antenna of CryoSat. Such an algorithm that takes the sensor data (level 1b data) from a satellite and computes geophysical parameters (or, level 2 data) is known as a level 2 Processor. This chapter discusses the developed CryoSat level 2 Processor by examining the different common retrackers presently used for retracking ice sheet radar returns, introduces the novel concept of *subwaveform* retracking and a brute force interferometric processing scheme that is designed to tackle phase ambiguities.

The chapter concludes with a brief explanation of the elevation change computation technique designed by Wouters *et al.* (2015), which has been adopted in a slightly modified form in this study.

3.1 THE DESIGNED CRYOSAT LEVEL 2 PROCESSOR

Before computing elevations, CryoSat SARIn data need to be preprocessed to remove waveforms that are contaminated with noise. Noisy waveforms have a much larger area under the curve (see Chapter 2) in comparison to waveforms that are much less noisy. This feature is exploited in our data-editing step. We compute the 'energy' of the waveform (or, the area under the curve of the waveform) using the Matlab function `trapz.m`. Observing the energy of multiple wave-

forms, we set a threshold. If the energy of the waveform exceeds this threshold, no elevations are estimated.

The full CryoSat level 2 processor designed in this study is summarised in Figure 16.

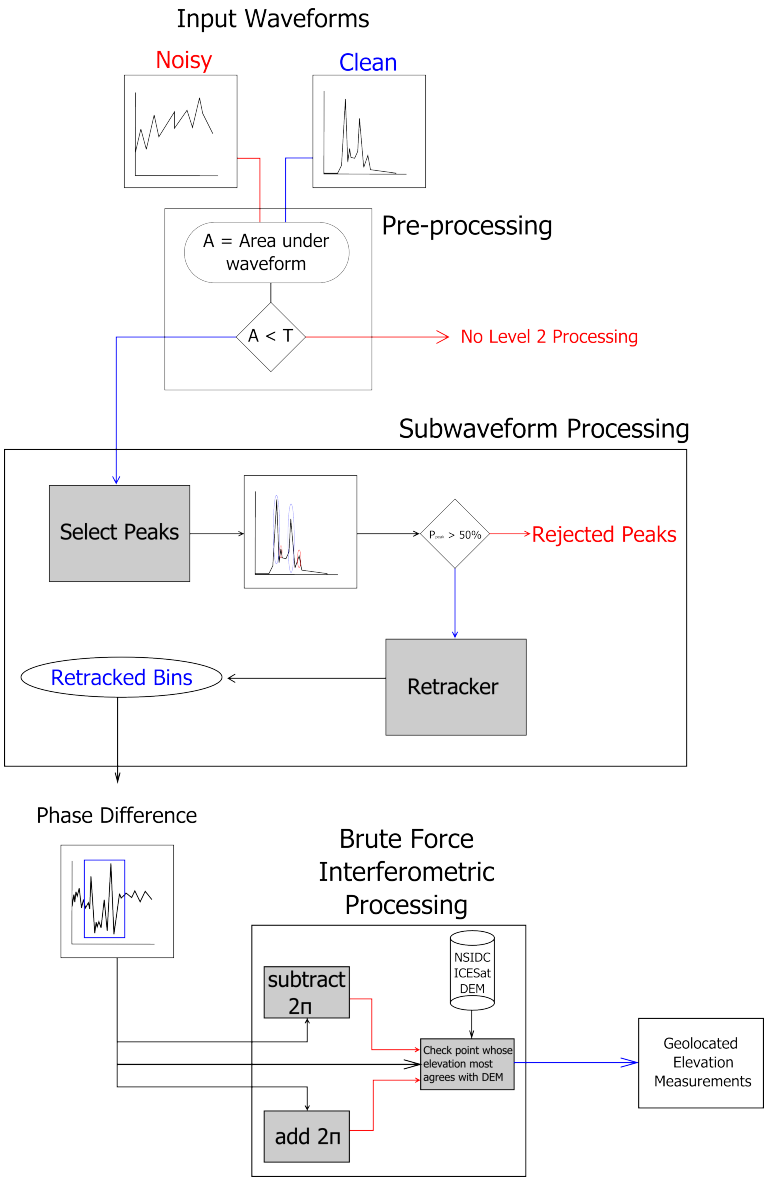

Figure 16: The flow diagram describes the level 2 processor designed to retrack and compute elevations and geo-locate scatterers from CryoSat SARIn waveforms. A and P_{peak} correspond to the 'Energy' of the waveform and the maximum power of the subwaveform, respectively. These parameters are computed to check whether the input waveform and the subwaveform peaks conform to the set threshold criterion.

3.2 RETRACKING

Retrackers are routines designed to locate the range bin that best represents the two-way travel time between the scattering *surface* and the satellite altimeter. With the help of retracking, it is possible to improve the accuracy of the measurements in the order of several meters. To demonstrate this, let us look at the principal equation involved in satellite radar altimetry,

$$R = \frac{c\tau}{2} \tag{3}$$

where, R, c, and τ are the range of the scattering surface to the satellite altimeter, the speed of light in vacuum, and the two-way travel time of the received pulse respectively. The two-way travel time, in the computation of the range, is fixed at the *Tracking bin* in Figure 17. The window delay is the theoretical two-way travel time of the received pulse and represents the t_0 in Figure 17. Taking the height of CryoSat relative to the WGS84 ellipsoid to be 717 km, we can calculate the theoretical two-way travel time 1_0,

$$t_0 = 7.15 \times 10^5 \times \frac{2}{c} \approx 0.0048\ sec$$

From Figure 17, the time $t_r - t_0$ is known as the retracker correction, where t_r is the time corresponding to the retracked bin location. So, the retracker correction t_{rc} is,

$$t_{rc} = t_0 - t_r. \tag{4}$$

Note that the time parameters in Equation 4 are computed with respect to the start of the tracking window.

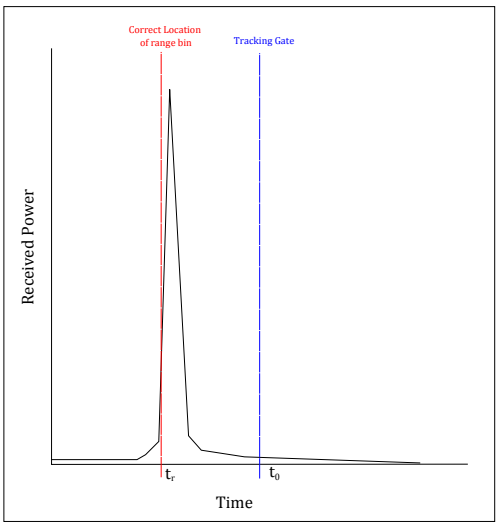

Figure 17: An example of a SARIn return over ice sheets. $t_0 - t_r$ represents the retracker correction that needs to be applied to obtain the correct two-way travel time.

Over ice sheets, CryoSat SARIn waveforms record the peak representing the POCA typically around bin 150. In CryoSat baseline B level 1B data products, the tracking bin/reference time is set at the 256^{th} bin (ESA & Laboratory, n.d.). So, effectively, the tracking bin at bin 256 is off by *106* bins from the range bin representing the scattering surface. In CryoSat's SARIn mode, each bin represents approximately 23 cm. So, in this case, the range measurement is corrected with approximately 24 m.

After obtaining the retracker correction, the next step is to compute the corrected range of the scatterer to the altimeter,

$$R_{corr} = \frac{c}{2}(t_{wd} - t_{rc}) + \triangle R_{\text{geophysical corrections}}, \tag{5}$$

where R_{corr} is the corrected range, t_{wd} is the *window delay* or the time from the signal transmission to the reference point on the waveform, and $\triangle R_{\text{geophysical corrections}}$ is a set of space/time dependent corrections. The geophysical corrections applied in this study are taken from the CryoSat level 1b data products. There are two main types of corrections, namely the atmospheric and the tidal corrections (ESA & Laboratory, n.d.). The atmospheric corrections are:

1. Dry Tropospheric Correction - Compensates for the effect of non-polar gases such as oxygen and nitrogen, and has a range of 1.7 - 2.5 m.

2. Wet Tropospheric Correction - Compensates for the effect of polar gases, mainly water vapour, and has a rang of 0 - 0.5 m.

3. Inverse Barometric Correction - Compensates for variations in sea surface height due to atmospheric loading, and has a range from -0.15 - 0.15 m.

4. Dynamic Atmospheric Correction - Compensates for variations in sea surface height due to atmospheric pressure and winds, and has a range from -0.15 - 0.15 m. This correction is only applied over open oceans.

5. Ionospheric Correction - Compensates for the slowing down of the radar pulses due to the pulse-free electron interaction in the ionosphere. The correction ranges from 0.06 - 0.12 m.

The tidal corrections are:

1. Ocean Tide Corrections - Corrections are provided for effects of local tides and long period equilibrium tides. These corrections range from -0.5 - 0.5 m.

2. Ocean Loading Tide Corrections - Removes the deformation of the Earth's crust due to the weight of the overlying ocean. The correction ranges from -0.02 - 0.02 m.

3. Solid Earth Tide Corrections - Removes the deformation of the Earth due to tidal forces from the Sun and the Moon acting on the Earth's body. The correction ranges fro -0.3 - 0.3 m.

4. Geocentric Polar Tide - Removes long period distortion of the Earth's crust caused by variations in centrifugal force as the Earth's rotational axis moves its geographic location. The correction ranges from -0.02 - 0.02 m.

In this research study, five different retrackers have been utilised. These are the, i) Threshold Retracker, ii) OCOG Retracker, iii) Gaussian fitting based Retracker, iv) Simplified CryoSat Retracker, and v) Beta Retracker. In the next section, all these retrackers are briefly introduced.

3.2.1 *Threshold Retracker*

The Threshold Retracker is a robust and simplistic approach to estimate the correct waveform bin associated with a ground scatterer in the received waveform by calculating the point that exceeds a particular chosen threshold. This threshold is represented as a percentage of the maximum received power in the waveform, and can be adjusted depending on the type of scattering (Davis, 1997). A small threshold

value is preferred when the received signal is dominated by volumetric scattering, whereas a high threshold is preferred for returns that are dominated by surface scattering.

To obtain the threshold-constrained tracking bin, this retracking technique considers three main parameters (Figure 18): i) the maximum power in the waveform P_{max}, ii) the thermal noise floor in the return waveform P_{noise}, and iii) the threshold coefficient C_t. Wingham *et al.* (2006) suggest that in SARIn waveforms, the point on the echo corresponding to the surface lies closer to the maximum. From this, we have chosen a threshold of 0.8. The exact received time t_r (Equation 4) is computed by a simple linear interpolation between the first sample below and after the threshold power, which is calculated by Equation 6.

$$P_{threshold} = P_{noise} + C_t(P_{max} - P_{noise}) \tag{6}$$

The parameters $P_{threshold}$, P_{noise}, and P_{max} are the power at the specified threshold, noise power and maximum power of the waveform, respectively.

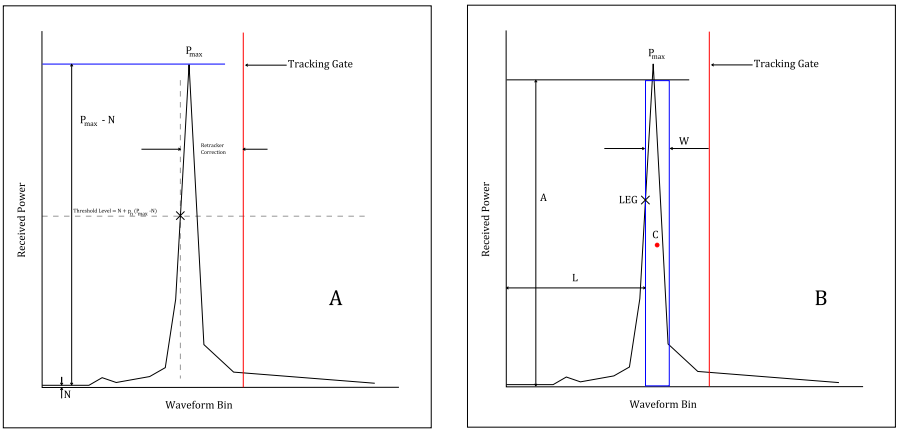

Figure 18: Figure A represents the threshold retracker and Figure B represents the OCOG retracker.

3.2.2 *OCOG Retracker*

The Offset Center of Gravity (OCOG) retracker is also an example of a method that is designed specifically for return echoes over ice sheets (Wingham *et al.*, 1986). This method is very robust as it does not require an analytical model to locate the leading edge of waveform peaks. The OCOG retracker uses the *energy* of the return waveform to assign a leading edge bin to the peak corresponding to the scattering surface. This is done by first computing the location of the *center of gravity* C (Figure 18 B) of the entire return waveform using Equation

7 . The energy, or the area under the waveform curve, is utilised as the area of a rectangle that is centered at this location. The width W is obtained from Equation 8.

$$C = \frac{\sum_{n=1}^{k} nP^2}{\sum_{n=1}^{k} P^2}, \tag{7}$$

$$W = \frac{(\sum_{n=1}^{k} P^2)^2}{\sum_{n=1}^{k} P^4}, \tag{8}$$

where P is the power at each bin of the return waveform, n is the bin number, and k is the total number of bins in the waveform. Finally, the leading edge epoch is computed using Equation 9,

$$t_r = dt\left(C - \frac{tW}{2}\right). \tag{9}$$

The Threshold and the OCOG retrackers belong to a class of retrackers known as statistical or numerical retrackers as they do not implement an analytical model to compute the leading edge position of a waveform peak. Due to this, statistical retrackers always provide a retracker result. Next, we will introduce some retrackers that belong to the class of so-called functional retrackers which use analytical models to obtain the leading edge position.

3.2.3 *Gaussian Retracker*

In the Gaussian retracking scheme, univariate multi-gaussian functions are fitted through the data to obtain an analytical representation of the waveform. This approach exploits the *Gaussian-like* shape of the peaks in the return waveform and fits eight different Gauss functions to the data. This number corresponds to the maximum number of Gaussian functions fit by Matlab's `fit` function. From visual inspection, we found that using the maximum number of Gaussian functions provided the best fit to the data. The functional model to be fit to the data is,

$$P = \sum_{n=1}^{8} a_n \exp\left(-\left(\frac{x - b_n}{c_n}\right)^2\right), \tag{10}$$

where P is the return waveform power at each bin, x is the bin number, n is the number of Gaussian functions, and a_n, b_n and c_n are the fit parameters of each of these Gaussian functions; i.e., the maximum received power, the location of the peak, and the width of the waveform peak. In total there are 24 parameters to be estimated.

n-parameters with a_n values over 50% of maximum power are selected and the tracking bin $n_{retracked}$ is located using Equation 11 and Equation 12.

$$n_{retracked} = b_n - c_n\sqrt{-\ln p_n}, \tag{11}$$

$$t_r = n_{retracked}\,dt, \tag{12}$$

where p_n is the threshold at which the tracking bin is expected, *dt* is the sampling interval. p_n depends on the type of scattering (see Section 3.2.1). Equation 11 is derived from Equation 13.

$$\begin{aligned} f(x) &= a\exp\left(-\frac{(x-b)^2}{c^2}\right) \\ \Rightarrow p_n a &= a\exp\left(-\frac{(x-b)^2}{c^2}\right) \\ \Rightarrow \ln(p_n) &= -\frac{(x-b)^2}{c^2} \\ \Rightarrow \ln(p_n)c^2 &= -(x-b)^2 \\ \Rightarrow x &= -\sqrt{-\ln(p_n)}c + b. \end{aligned} \tag{13}$$

3.2.4 *Simplified CryoSat Retracker*

Giles *et al.* (2007) designed the Simplified CryoSat Retracker as a simplification to the original CryoSat retracker designed by Wingham *et al.* (2006). In this retracker the return waveform is split into three parts: i) the leading edge governed by a Gaussian function, ii) a polynomial function that represents the top of the peak of the waveform, and iii) an exponential trailing edge that is described by the following function,

$$P = a\exp^{-f^2(t)}, \tag{14}$$

where a is the maximum return waveform power, and

$$f(t : t < t_a) = \frac{t - t_a}{\sigma} \tag{15}$$

$$f(t : t_a < t < t_a + t_b) = \frac{t - t_a}{\sigma} + a_2(t - t_a)^2 + a_3(t - t_a)^3 \tag{16}$$

$$f(t : t > t_a + t_b) = \sqrt{k(t - t_a)} \tag{17}$$

t_a is the bin corresponding to the maximum amplitude a, k is the rate of decay of the trailing edge, σ is the width of the leading edge (or, standard deviation of the Gaussian function), t_b is the distance between the leading and the trailing edges, and a_2 and a_3 are constants.

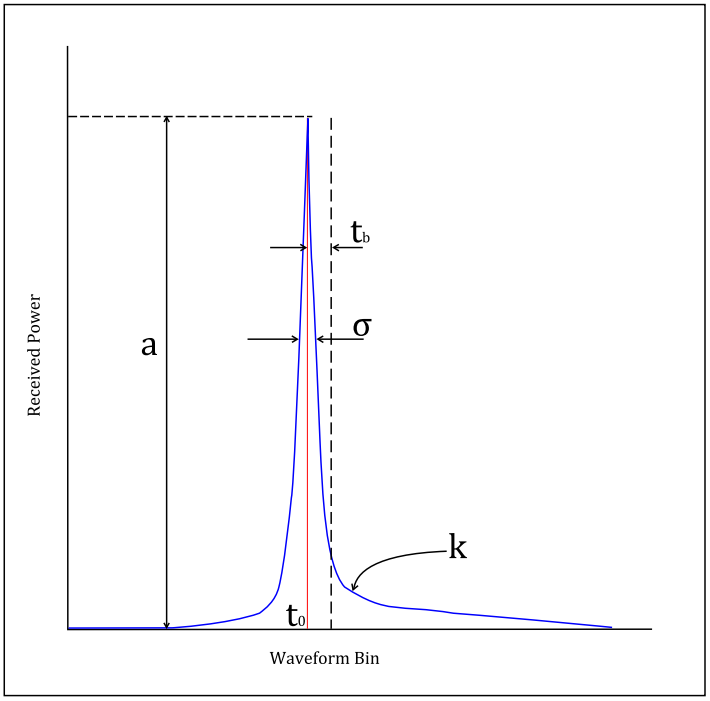

Figure 19: The primary motivation to design the simplified CryoSat retracker was to reduce the number of parameters involved in retracking SARIn waveforms using the original CryoSat retracker. In comparison to the original CryoSat retracker The Simplified CryoSat Retracker reduces the number of segments in the waveform from five different segments to just three.

The constants a_2 and a_3 are chosen such that P and its first derivative are continuous and smooth (Stenseng, 2011);

$$a_3 = \frac{(-\sqrt{kt_b}2\sigma/t_b) + 2}{(t_b^2 + 2t_a^2 + 2t_a t_b(3 - 2\sigma)}, \tag{18}$$

$$a_2 = \frac{\sqrt{kt_b}}{t_b^2} - \frac{1}{\sigma t_b} - a_3 t_b. \tag{19}$$

After estimating the parameters by using non-linear regression, t_a is used as the corrected tracking bin. In this research, we also use a separate method to obtain the leading edge tracking bin by using Equation 20.

$$\begin{aligned} n_{\text{retracked}} &= t_a - \sigma\sqrt{-\ln p_n}, \\ t_r &= n_{\text{retracked}}\, dt. \end{aligned} \tag{20}$$

The parameter p_n is the *threshold* or the fraction of the maximum power at t_a where the leading edge bin is expected.

3.2.5 *Beta Retracker*

The Beta retracker (Martin *et al.*, 1983) was the first attempt to retrack radar altimeter returns over ice sheets. The retracker is based on the famous Brown's ocean model (Brown, 1977).

$$P(t : t \geqslant 0) \approx \eta_P P_T P_{fs} \sqrt{2\pi}\sigma_P \frac{1}{2}\left[\operatorname{erf}\left(\frac{t}{\sqrt{2}\sigma}\right) + 1\right] \tag{21}$$

The Brown's model draws a relation between the received power by a radar altimeter to geophysical parameters like the ocean surface elevation density function, and the SWH or the Sea Wave Height. The Beta retracker model uses empirical analogues of the various parameters in the Brown's model (Equation 22):

$$P(t) = \beta_1 + \beta_2(1 + \beta_5 Q) f\left(\frac{t - \beta_3}{\beta_4}\right), \tag{22}$$

where

$$f(z) = \frac{1}{\sqrt{2\pi}} \int_{-\infty}^{z} \exp^{\frac{-q^2}{2}} dq, \tag{23}$$

$$Q = \begin{cases} 0 & t < \beta_3 + \frac{\beta_4}{2} \\ t - \left(\beta_3 + \frac{\beta_4}{2}\right) & t \geqslant \beta_3 + \frac{\beta_4}{2} \end{cases}, \tag{24}$$

β_1 represents the thermal noise in the return waveform, β_2 is the return power, β_3 is the midpoint of the leading edge, β_4 is the leading edge rise time, and β_5 represents the slope of the trailing edge. The term q in Equation 24 (the erf function with a lower bound of $-\infty$ to $z = \left(\frac{t-\beta_3}{\beta_4}\right)$) represents Q. It is important to note that this specific retracker was designed for the SeaSat altimeter that had a low trailing slope in the received waveform *ramps*, or peaks. The retracker was later revised with an exponential trailing edge (Deng & Featherstone, 2006). The revised Beta retracker has been implemented in this study,

$$P(t) = \beta_1 + \beta_2 \exp^{-\beta_5 Q} f\left(\frac{t - \beta_3}{\beta_4}\right), \tag{25}$$

where

$$Q = \begin{cases} 0 & t < \beta_3 + k\beta_4 \\ t - (\beta_3 + k\beta_4) & t \geqslant \beta_3 + k\beta_4 \end{cases}. \tag{26}$$

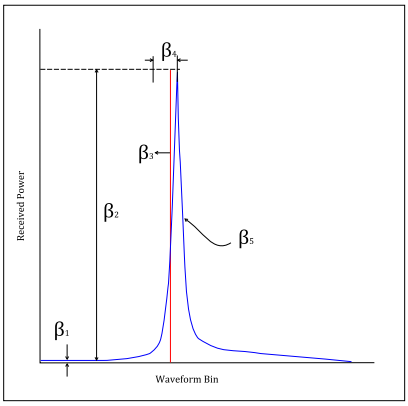

(a) The different β-parameters in the waveform from the Deng & Featherstone (2006) updated beta model

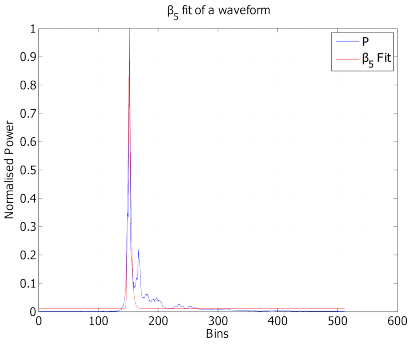

(b) Example of a fit by the updated beta-5 retracker using the levenberg-marquardt least squares implementation of Matlab

Figure 20: The Beta-5 retracker

In this study, the parameter k locates the beginning of the trailing edge and is estimated along with the other parameters. The β_3 parameter locates the retracking bin t_r (Equation 4). The beta-5 retracker only retracks the POCA. The beta-9 retracker was introduced to retrack waveforms with two distinct peaks (Martin *et al.*, 1983):

$$P(t) = \beta_1 + \sum_{i=1}^{2} \beta_{2i} \exp -\beta_{5i} Qf\left(\frac{t - \beta_{3i}}{\beta_{4i}}\right), \tag{27}$$

where

$$Q_{i:i=1\to2} = \begin{cases} 0 & t < \beta_{3i} + k\beta_{4i} \\ t - (\beta_{3i} + k\beta_{4i}) & t \geqslant \beta_{3i} + k\beta_{4i} \end{cases} \tag{28}$$

The beta-9 retracker provides information about an additional reflecting surface apart from the POCA.

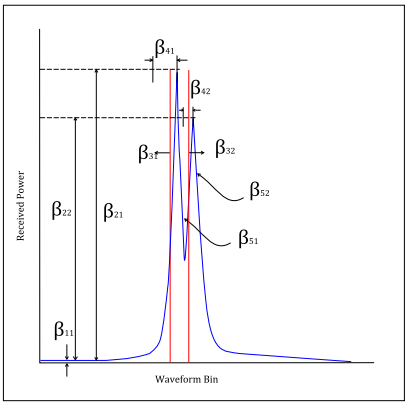

(a) The different β-parameters in the waveform from the Deng & Featherstone (2006) updated beta model

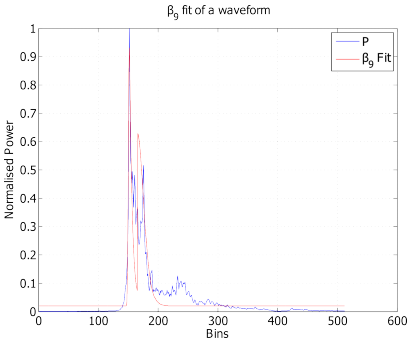

(b) Example of a fit by the updated beta-9 retracker using the levenberg-marquardt least squares implementation of Matlab

Figure 21: The Beta-9 retracker

3.2.6 *Retracker modification : A multiple sub-waveform approach*

Distinct scatterers within a radar footprint that contribute to the received waveform share similar features — they all possess a leading edge, a trailing edge, and a local maxima that lies in between the leading and the trailing edge. These features are observed for almost all waveforms and only differ for cases of data contaminated with noise.

We exploit this by introducing the concept of sub-waveform retracking. In this approach, individual peaks in the return waveform are separated into *sub-waveforms*, and their leading edges are retracked individually. The steps followed are,

1. *Locate peaks in the received waveform.*

   The waveform peaks are located by Matlab's `findpeaks` routine. We choose a peak separation of 20 bins in order to accommodate the trailing edge of the previous slope, the leading edge of the current slope and the trailing edge of the current slope.

2. *Remove all peaks with maximum receive power of less than 50% of the global maximum.*

   This step is necessary to only retrack peaks that return a significant amount of return power with respect to the global maximum.

3. *Reject all peaks that appear too soon (before bin number 40) or too late (after bin number 500).*

   From preliminary inspection of various waveforms, it is observed that the peak representing POCA falls somewhere around bin 150. However with noisy waveforms, it is possible to find

peaks before bin 40. Peaks beyond bin 500 are usually observed in very noisy waveforms.

4. *Isolate sub-waveforms by selecting five bins around the bin representing the local maximum.*

5. *Apply statistical or functional retracker.*

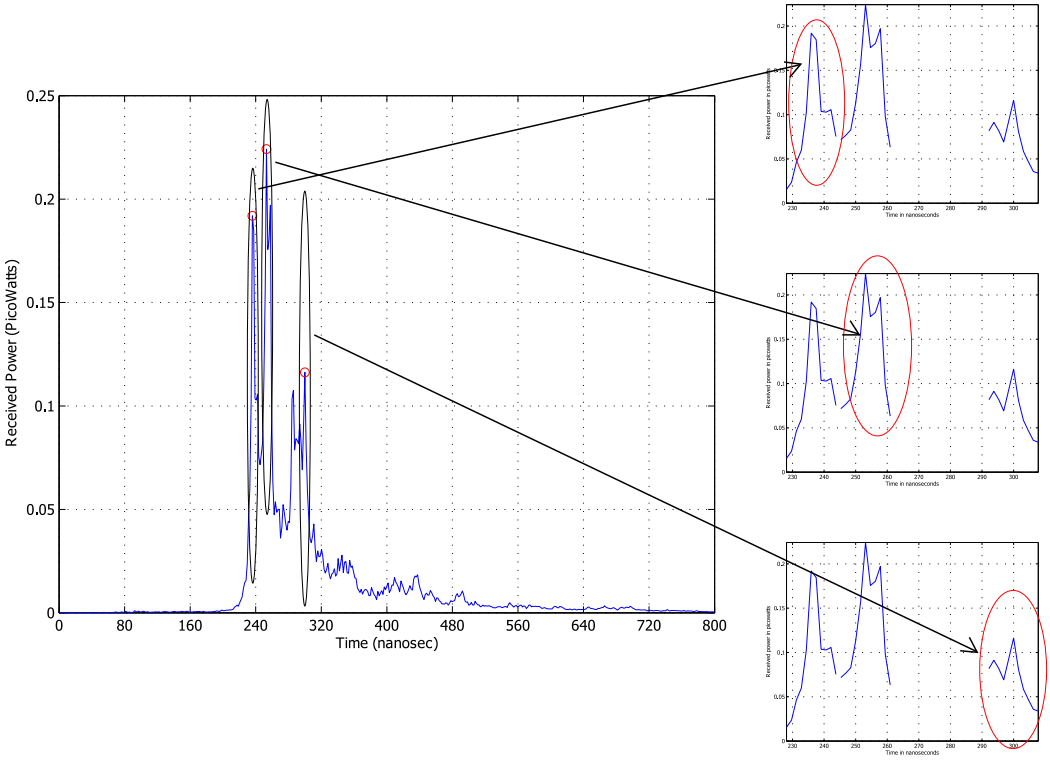

Figure 22: From the waveform in this example, there are three *peaks* that match the criteria discussed in Section 3.2.6. In the subwaveform approach, each of these separate peaks is retracked independently from each other. From this example, we observe that the third peak may not be retracked successfully, i.e., the retracking point could be located ouside the leading edge of the peak due to the presence of a sub-peak. This is because some retracking techniques may not respond well to *noise* on the leading edge.

Scatterers beyond the POCA are retracked using the subwaveform approach. If the data only contain valid single-peak waveforms, our results will provide the same number of retracked peaks as the number of waveforms. If the number of valid peaks per waveform is greater, our results will provide more retracked peaks than the number of waveforms. The next section discusses the modified retrackers that have been implemented in this study.

3.2.7 *Implemented Retrackers in this study*

In this study, eight different retrackers are implemented. These are based on the five retrackers discussed in Section 3.1.1 - 3.1.5, and the subwaveform approach:

1. The Multi-Threshold Retracker is a subwaveform retracker that applies the Threshold Retracker to individual subwaveforms to obtain multiple retracked peaks in a SARIn waveform. A threshold coefficient value of 0.8 is used.

2. The Multi-OCOG Retracker is a subwaveform retracker that applies the OCOG Retracker to individual subwaveforms to obtain multiple retracked peaks in a SARIn waveform.

3. The Beta Retracker.

4. The Multi-Gauss Threshold Retracker utilises the Gaussian retracker and the subwaveform approach:

   (i) An 8-Gaussian function is fit to the waveform.

   (ii) The subwaveform approach is applied to the fit.

   (iii) The Threshold retracker with a threshold coefficient value of 0.8 is applied to the subwaveforms.

   This method has been designed to test the feasibility of using functional fits of waveforms and statistical retrackers in tandem. Helm *et al.* (2014) implemented a similar approach, where they used a modified version of the Threshold retracker to a smoothened SARIn waveform, to obtain the leading edge of the waveform.

5. The Multi-Gauss OCOG Retracker follows the same process as the Multi-Gauss Threshold Retracker with the exception that it uses the OCOG retracker instead of the Threshold retracker.

6. The Gauss Retracker utilises the Gaussian retracker and Equation 11 to obtain multiple retracked bins in the waveform:

   (i) The Gaussian retracker isapplied, resulting in 24 different fit parameters.

   (ii) Fit parameters (a_n, b_n, and c_n) with $a_n > 50\%$ of the maximum power are selected.

   (iii) Leading edges of the waveform peaks are located by implementing Equation 11.

7. The Multi-Simplified CryoSat Retracker is our implementation of the Simplified CryoSat Retracker designed by Giles *et al.* (2007), designed to retrack multiple peaks. This retracker utilises the

subwaveform approach for providing peak locations and compiling initial values for fitting. The steps are outlined as follows:

(i) The subwaveform approach is applied to identify all waveform peaks.

(ii) For each subwaveform, the initial values are computed for each parameter in Equation 14.

(iii) The function to be fit is compiled from these fit parameters. This compilation is done by summing Equation 14 for each peak. Such a functional model was compiled for the beta-9 retracker.

(iv) The functional model is fit to the waveform using the 'trust-region-reflective' option of Matlab's `lsqcurvefit.m` function.

(v) The retracked bins are assigned to the waveform.

8. The Multi-Simplified CryoSat II Retracker is our subwaveform implementation of the Simplified CryoSat Retracker that utilises the Gaussian-like leading edge fit parameters for locating the location of the leading edge. The difference of this method with the Multi-Simplified CryoSat Retracker is that it does not utilise the subwaveform approach to compute initial values. Rather, the method fits the subwaveforms itself. This method follows these steps:

(i) The subwaveform approach is applied to get the subwaveforms.

(ii) The Simplified CryoSat model (Equation 14) is applied to these subwaveforms.

(iii) From the subwaveforms, the retracker bin is obtained by applying Equation 20 with a threshold (p_n) of 0.8.

3.3 THE BRUTE-FORCE INTERFEROMETRIC PROCESSING APPROACH

The phase difference of the signal received by the two antennae for each epoch in the return waveform is computed and stored in the level 1b dataset. Using these data and the knowledge of the retracked bin on the received waveform corresponding to a scattering surface, the phase difference for that peak is computed.

The phase difference of the received signal between the two antenna lies within a range of $[-\pi, \pi]$. Helm *et al.* (2014) observed that for scatterers lying beyond an off-nadir angle of 0.54° with respect to the satellite, the phase difference jumps beyond this range and is wrapped to fit into the $[-\pi, \pi]$ range. In fact, three different cases can be distinguished:

1. If the scatterer is positioned at a flat surface within a distance of approximately $R \sin\theta = 717 \text{ km} \times \sin(0.54) \approx 6.75 \text{ km}$ from the nadir point in across track direction, the phase difference data is not wrapped.
2. If the scatterer lies at a larger off-nadir angle, and the phase difference is wrapped.
3. If the scatterer is positioned on a very steep across track slope, the phase difference is wrapped (ESA, 2014).

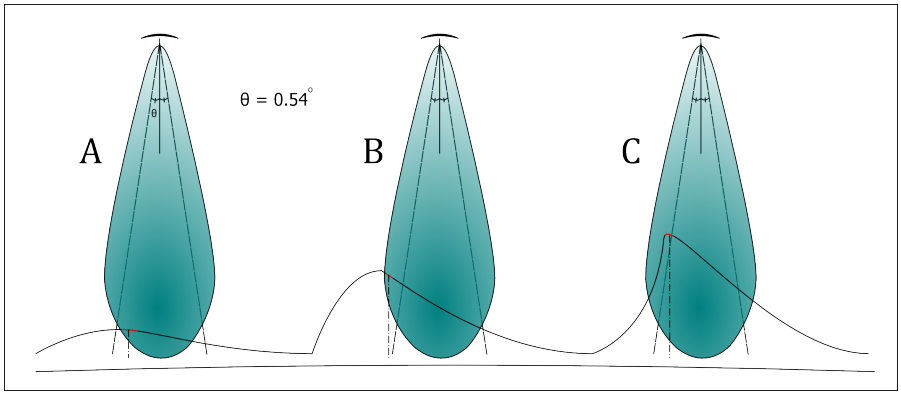

Figure 23: In scenario *A*, The scatterer is within an off-nadir angle of 0.54° and the interferometric phase difference does not get wrapped. Scenario B represents a case of when the off-nadir angle of the scatterer is larger than 0.54°. Scenario C is the situation when the scatterer is located within this 'no-wrap' off-nadir angle, but the phase is still wrapped due to very steep across track slope.

Without the use of external information, it is impossible to resolve this ambiguity. In this study, the 1 km x 1 km GLAS/ICESat Digital Elevation Model from DiMarzio *et al.* (2007) is utilised to correct for this ambiguity. This DEM is converted from its Polar Stereographic coordinate system to the geodetic latitude and longitude using routines obtained from MATLAB Central (Bliss, 2011). The procedure for interferometric processing comprises the following steps:

1. The retracked bins are rounded to the nearest integer and the phase data ϕ for that bin are assigned to the scatterer.
2. It is unknown whether the phase data has been wrapped. So, three interferometric phase difference scenarios are realised: i) $\phi - 2\pi$, ii) ϕ, and iii) $\phi + 2\pi$.
3. The interferometer angle θ (or, the off-nadir angle) is obtained by the following expression:

$$\theta = F_c \sin^{-1}\left(\frac{(\phi + k)\lambda}{2\pi B}\right), \tag{29}$$

where B is the baseline of the altimeter, $k = [-2\pi, 0, 2\pi]$, λ is the wavelength of the transmitted signal and $F_c = 1/0.973$ is a correction to be applied in the calculation of the interferometer angle (Galin *et al.*, 2013).

4. The range of the satellite to the scattering surface is computed using Equations 3 to 5.

5. The across-track ground range from the nadir and the elevation of the scatterer with respect to the WGS 84 ellipsoid is computed using (Figure 24):

$$R_{\text{ground range}} = R_{corr} \sin\theta, \tag{30}$$

$$h_{\text{scatterer}} = \left[h_{sat} - R_{corr}\cos\theta + R_E\left\{1 - \cos\left(\frac{R}{R_E}\theta\right)\right\}\right]\cos\left(\frac{R}{R_E}\theta\right). \tag{31}$$

6. With the known nadir point location and the calculated ground ranges for three different *possibilities* of phase, three possible locations of the scatterer are computed. This is facilitated by computing the azimuth of the satellite track from the Matlab function `azimuth.m`, and locating the scatterer using the ground range and the `reckon.m` function. All computations are done with respect to the WGS 84 ellipsoid.

7. Using linear interpolation, the NSIDC DEM values at the three different positions per retracked range are calculated and compared to the computed elevations. The position that corresponds to the elevation that agrees best to the interpolated DEM is selected as the most likely position of the scatterer.

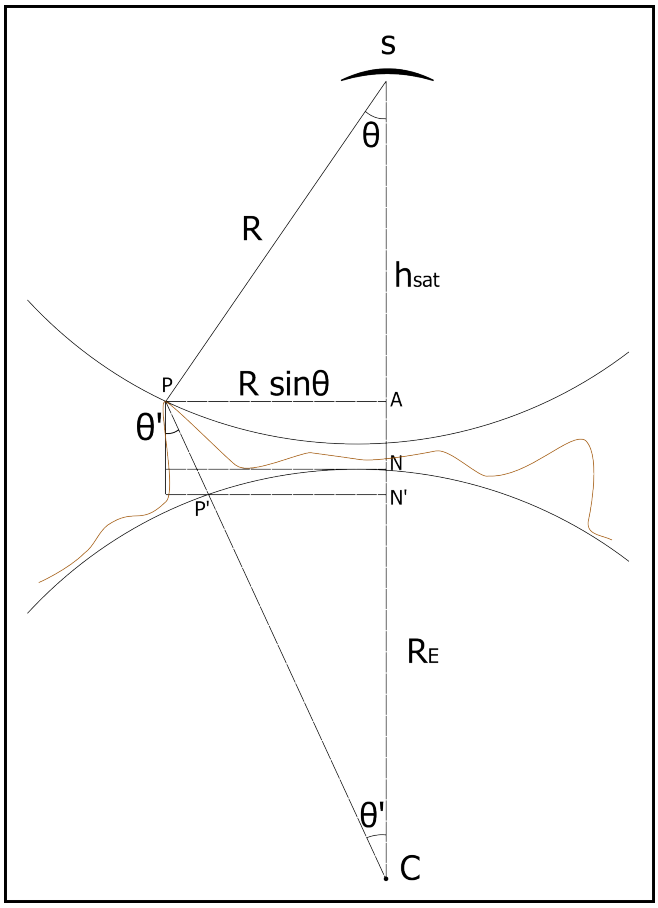

Figure 24: Elevation computation geometry for level 2 Processor designed in this study. Parameters $R, R_E, \theta, \theta', \text{and } h_{sat}$ represent the range of the scatterer to the satellite (SP), the mean radius of the Earth (CN), the interferometer angle $(\angle ASP)$ and the angle $(\angle NCP')$ subtended by the arc NP', which joins the nadir point N and the scatterer's position on the ellipsoid P', at the center of the Earth C, respectively. The elevation of the scatterer $PP' = AN' \cos\theta'$, where $\theta' = \frac{R}{R_e} \cos\theta$, and $AN' = AN + NN' = (h_{sat} - R\cos\theta) + (R_E - R_E \cos\theta')$. AP is the ground range. The figure is not drawn to scale.

3.4 SURFACE ELEVATION CHANGE MEASUREMENT USING MEASUREMENT GROUPING

The study's primary objective is to get the most information out of CryoSat level 1b SARIn waveforms to study the Greenland's ice sheet elevation changes. This section discusses our modified version of Wouters *et al.* to obtain ice sheet elevation change information. The method comprises of four steps:

1. For each measurement point (referred to as the central point), all data points within 0.0045° latitude and longitude from the central point are selected (including the central point) using the Matlab's `ingeoquad.m`.

2. The selected points are checked for outliers by implementing the iterative Grubbs test. This implementation was provided by Shoelson on Matlabcentral. If the central point is removed from this iterative outlier detection scheme, the process is stopped, and no elevation change is computed for that point.

3. To compute reliable elevation trends, three criteria are set for the grouped data points:

   (i) Total number of data points $\geqslant 12$;

   (ii) The data points should belong to at least three different satellite passes;

   (iii) The time span covered by the data should be at least two years.

   If the criteria are not met, the process is stopped and no elevation change is computed for that central point.

4. A 9-polynomial surface model is fit along with the linear trend parameter (Wouters *et al.*, 2015),

$$\begin{aligned} Y = a_1 + a_2 t + a_3 x + a_4 y + a_5 x^2 + a_6 y^2 + a_7 xy \\ + a_8 x^2 y + a_9 x y^2 + a_{10} x^2 y^2, \end{aligned} \tag{32}$$

   where Y contains the elevations the data points in the group, parameters $a_1 - a_9$ are to be estimated, t is the measurement epoch (in years), and x and y are the longitude and latitude respectively. The estimation is carried out using Matlab's nonlinear regression function `nlinfit`. The estimated linear trend parameter a_2 is assigned to the centroid of the selected data points. This centroid location is computed by taking the average of the positions of the selected data points.

We implement the following modifications compared to the method designed by Wouters *et al.* (2015):

1. A latitude-longitude constraint of 0.0045° is chosen to select data points around the central measurement point, instead of clustering data points within 500 m to the central point. This step decreases the computation time.

2. The 1-D elevation change trend is assigned to the centroid of the selected data points, instead of the central point.

3.5 CONCLUSION

In an effort to utilize the full waveform information, we designed a novel subwaveform approach that enables retracking of multiple scattering surfaces in the SAR footprint. From this subwaveform approach, we provide six different multi-peak retrackers, and two other retrackers for testing purposes. Such an approach is the first attempt to retrack multiple scatterers from a single SARIn waveform.

Because the SARIn phase difference data can be ambiguous, we designed a brute force interferometric approach that looks at the possibilities of elevations and ground locations and compare them to a reference DEM. The elevation and ground location combination that agrees best with the reference DEM is assigned as the final level 2 product. Indeed, the accuracy of the results will strongly depend on the quality of the reference DEM begin used.

The next chapter discusses the results obtained from the application of these methods, provides a qualitative comparison of the different retrackers implemented, and explains the elevation change information computed over the Jakobshavn Isbræ.

4

RESULTS AND DISCUSSION

To assess the performance of the (subwaveform) retrackers, all designed methods were applied to derive the elevation changes over the Jakobshavn Isbræ.

Hurkmans *et al.* (2012b), Helm *et al.* (2014), and Thomas *et al.* (2009) observed a clear elevation change signal over the Jakobshavn Isbræ, concentrated at the mouth of the glacier. Based on their map, we generate a polygon the region of interest (see Figure 25).

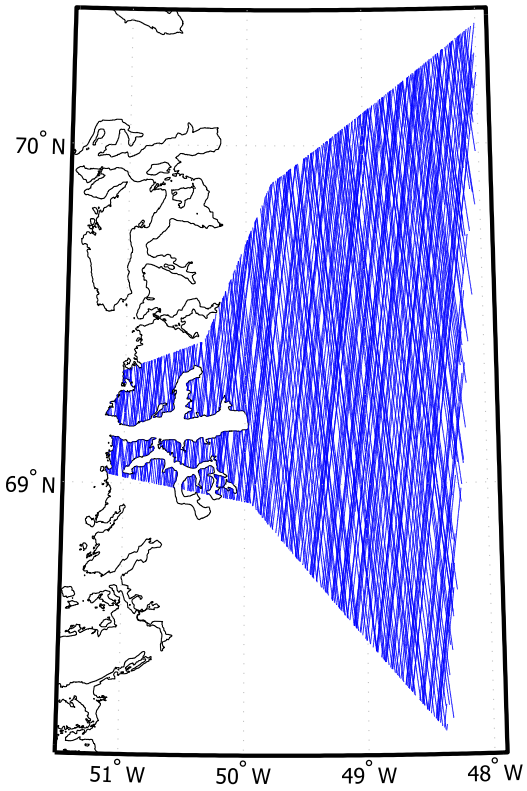

Figure 25: Jakobshavn Isbrae - The blue lines represent CryoSat satellite tracks on SARIn mode between 2010 and 2015

This chapter assesses the performance of each of these methods by comparing the computed elevations to i) the available level 2 CryoSat data over the basin and, ii) the ICESat DEM by DiMarzio *et al.* (2007). The chapter also compares the linear elevation change trends computed over the chosen region to the values available in scientific literature.

4.1 JAKOBSHAVN ISBRAE - SOME FACTS

The Jakobshavn Glacier, or the Jakobshavn Isbrae in Danish, is a marine terminating glacier terminating at Ilulissat Icefjord in West Greenland. It is the largest and the fastest outlet glacier of Greenland and handles the drainage of about 5.4% - 6% of the surface area of Greenland ice sheet (Motyka *et al.*, 2011; Echelmeyer *et al.*, 1993). The fluctuating velocity of the glacier is the subject of various scientific studies. Between 1985 to 1992, the glacier slowed down from 6700 m/yr to 5700 m/yr and then sped up to 9400 m/yr by the year 2000. A speed up to 12,600 m/yr in 2003 was reported by Joughin *et al.* (2004), which increased to 18,000 m/yr in 2014 (Messerli *et al.*, 2014). This acceleration of flow in 1998 was accompanied by the progressive increase in the retreat of the glacier. Luckman & Murray (2005) speculated that the initiation of this acceleration and retreat may have been driven by the same mechanism that led to the departure of the seasonal glacier flow rate invariance in spring 1995.

What is most relevant to our study, however, is the rapidly changing surface elevation of the Glacier. Prior to 1997, Jakobshavn was one of the few glaciers to observe a thickening trend (Thomas *et al.*, 2009), after which it began thinning at alarming rates. Between 1997 - 2006, the glacier has experienced thinning at the rates higher than 20 m/yr (Hurkmans *et al.*, 2012b).

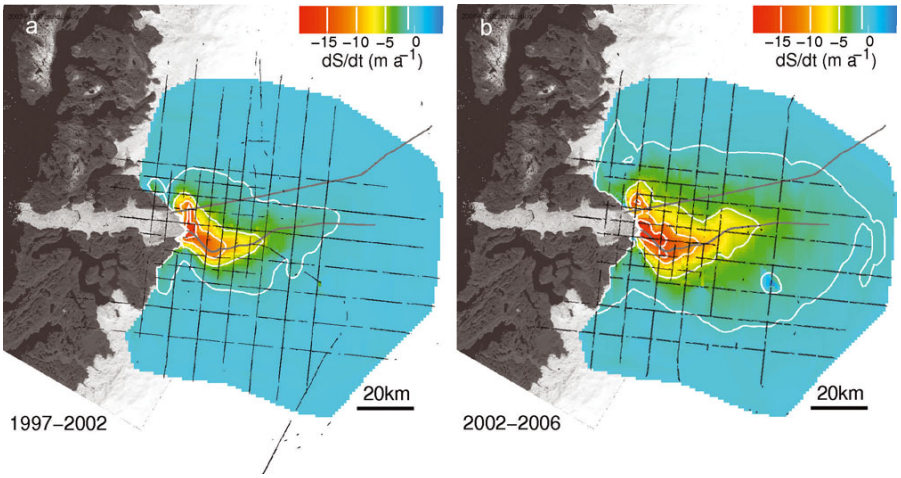

Figure 26: The figure describes the spatial pattern of the thinning observed in JakobShavn from ATM (*Airborne Topographical Mapper*) flights, overlayed over a Landsat image from 2002. Image adapted from Thomas *et al.* (2009).

Holland *et al.* (2008) provided hydrographic data that showed an increase in subsurface ocean temperatures along the west coast of Greenland. They suggested that the increase in acceleration and thinning of the Jakobshavn Isbræ could be explained by:

i) Increased lubrication of the ice-bedrock interface with an increase in meltwater drained to the glacier bed due to increasing summer temperatures.

ii) Weakening and break-up of the floating ice tongue that buttressed the glacier.

Holland *et al.* further noted that the increase in ocean temperatures along West Greenland originated from the Irminger Sea near Iceland, which provided warm waters to the coastal zone. This oceanic circulation change was traced to the changes in the atmospheric circulation of the North Atlantic region.

4.2 CRYOSAT LEVEL 2 ELEVATIONS FROM DESIGNED PROCESSOR

This section discusses the results derived from the designed level 2 processor from this project and compares it to the CryoSat ESA level 2 data products and the ICESat (Ice, Cloud, and land Elevation Satellite) digital elevation model from DiMarzio *et al.* (2007).

4.2.1 *CryoSat Level 2 products from ESA*

There is a total of 141,788 points (corresponding to an equal number of SARIn waveforms) in the ESA-CryoSat level 2 data over the Jakobshavn basin outlined in Figure 25 acquired over the period 2010-2015. These data were downloaded from the CryoSat FTP server using a downloader developed in `Python`. The retracking method used in this processor is known as the CryoSat Retracker (Wingham *et al.* (2006)) which is designed to retrack a single peak in the received pulse waveform. Figure 4 represents a map of elevations. The data have not been post-processed.

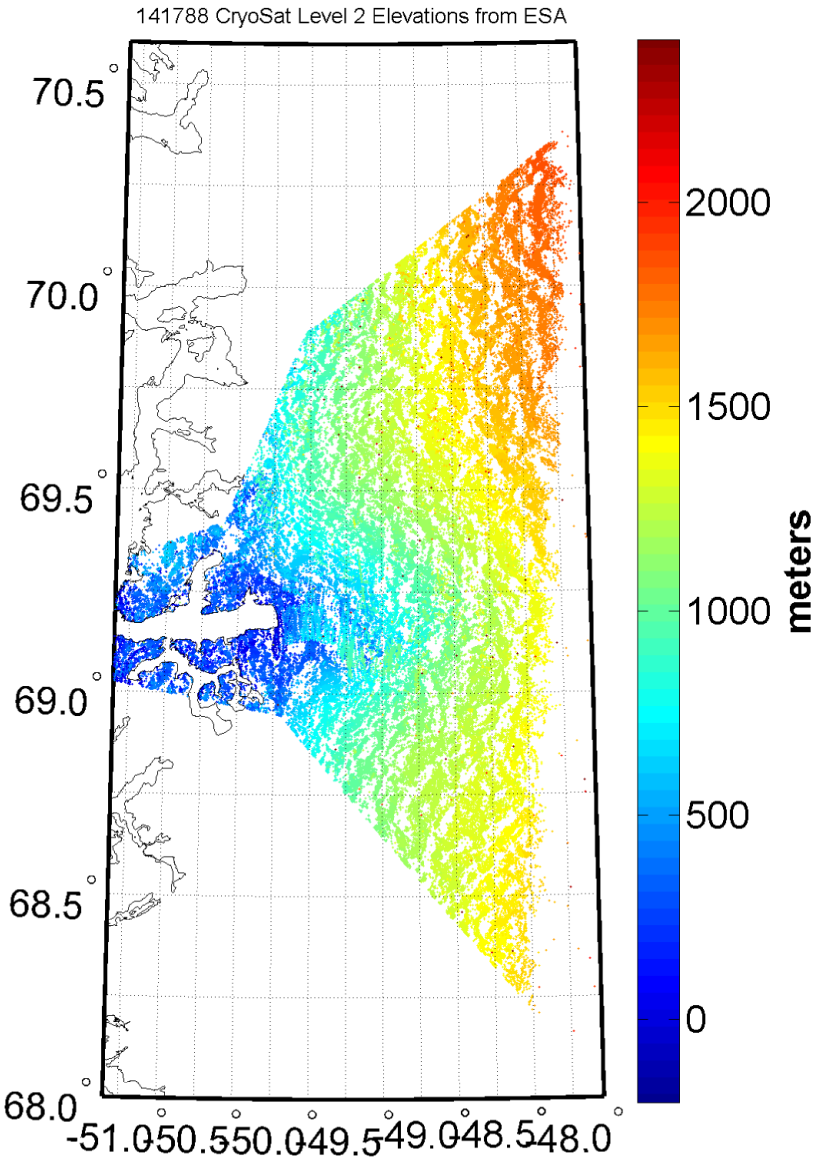

Figure 27: This map represents the data from the CryoSat level 2 retracker. The elevations are with respect to WGS 84 ellipsoid.

4.2.2 *Results from different retrackers*

Upon downloading CryoSat Level1b data for the same region described in Figure 25 and the same period, a total of 132,155 CryoSat SARIn waveforms were found, which is different from the number of waveforms in level 2 data. The reason of this discrepancy is unknown.

In Table 2, the results from retracking 588 CryoSat satellite tracks over the Jakobshavn basin are provided. The retracked data starts at the beginning of the satellite mission in 2010 to March 2015.

Table 2: The parameters n_{POCA}, $n_{non\text{-}POCA}$, and n_{total} represent the number of retracked points from the POCA, the number of retracked points beyond the POCA and the total number of retracked points by the retrackers described in Section 3.1.7. The retracker names are abbreviated: i) m-T is multi-Threshold, ii) m-OCOG is multi-OCOG retracker, iv) m-GT is multi-Gauss Threshold, v) m-GOCOG is multi-Gauss OCOG, vii) m-SC is multi-Simplified CryoSat, and viii) is the multi-Simplified CryoSat II retrackers.

Name	n_{POCA}	$n_{non\text{-}POCA}$	n_{total}
m-T	129762	162983	292745
M-OCOG	129762	162983	292745
Beta	82929	36246	119175
m-GT	129613	104037	233650
m-GOCOG	129613	104037	233650
GS	129737	33284	163021
m-SC	129762	162983	292745
m-SCS	115313	138633	253946

4.2.2.1 *Discussion of results from retracking*

Possibly the most important observation that can be made from Table 2 is the total number of retracked waveform peaks. A very high number of peaks that lie beyond the POCA (non-POCA) are retracked. Just from retracking these peaks, the number of elevation estimates becomes approximately twice the number of elevation estimates from a level 2 processor that does not look beyond the peaks that represent the point of closest approach.

Every multi-peak retracker works with the same number of sub-waveforms in a received waveform. However, the total number of retracked bins are different for each retracker because of the different computation methods. The following observations and conclusions are drawn from Table 2:

1. **The Multi-Threshold, Multi-OCOG, and Multi-Simplified CryoSat retrackers provide the maximum number of retracked peaks.**

   The Threshold and the OCOG retrackers are empirical retrackers that benefit from the subwaveform approach, which gives these retrackers the opportunity to retracker all possible peaks in a waveform. The approach provides the Multi-Simplified CryoSat retracker with the initial conditions for carrying out the analytical fits for the same number of subwaveforms as the Multi-Threshold and the Multi-OCOG retrackers.

2. **The Beta Retracker provides the smallest number of retracked peaks.**

   The Beta Retracker is designed to only retrack one peak that lies beyond the first peak in the received pulse waveform. Because of this, the maximum number of points that can be retracked from a single received waveform is 2. Also, the Beta Retracker relies on an analytical model to locate the leading edge of the peaks . If a waveform is very noisy, it will affect the output of the fitting routine. Due to these 'limitations', the total number of retracked peaks by the Beta Retracker is the lowest compared to the number obtained using the other retrackers.

3. **Among the multiple scatterer retracking techniques (except the beta retracker) the Gaussian retrackers show a different number of retracked POCA and non-POCA points.**

   Because the Gaussian fits of the received waveform do not completely resemble the original waveform, the number of peaks present in the fitted waveform changes. This implementation was designed with the assumption that the shape of a peak in the return waveform resembles that of a Gaussian function. However, this is not the case for all received waveforms. In many cases, the fitted waveform represents a smoothened version of the waveform that does not represent the exact number of 'valid' peaks as the original waveform. This results in a decrease in the total number of retracked peaks.

4.2.3 *Elevations computed after Interferometric Processing of retracker results*

To assess the performance of the different retrackers, the ICESat DEM (DiMarzio *et al.*, 2007) is utilized. Using the Matlab's `scatteredInterpolant`, the DEM was linearly interpolated to the positions where the level 2 processor outputs results. After that, the interpolated DEM elevation value is subtracted from the level 2 processor elevation. The statistics of these differences are shown in Table 3. The results in the table have been post-processed by applying an implementation of the Grubb's

test for outlier detection and removal. This test is an iterative outlier detector that computes a test statistic using the data in a sample with the maximum deviation. This test statistic is compared to a computed critical value computed from the data sample. From this comparison, it is decided whether an observation is accepted or rejected (Grubbs, 1969).

Table 3: Statictics of the elevation differences between ICESat and L2 processed data (in m). The table contains the total number of POCA points n_p, the total number of non-POCA points n_{np}, the total number of points n_t, the mean difference of elevation from NSIDC ICESat DEM at these POCA retracked points μ_p, the standard deviation of this difference at POCA σ_p, the mean of the difference from the NSIDC ICESat DEM for points beyond the POCA μ_{np} and the standard deviation of this difference σ_{np}. L2ESA is the shortened name of level 2 ESA products.

Name	n_p	n_{np}	n_t	μ_p	σ_p	μ_{np}	σ_{np}
m-T	122125	152434	285422	-4.29	48.45	-11.81	35.82
m-OCOG	122176	152406	285549	-4.14	48.36	-11.92	35.02
Beta	79612	33941	116151	-0.70	66.24	-11.81	38.80
m-GT	121949	97628	227649	-5.46	47.62	-11.65	36.91
m-GOCOG	126459	97662	227868	-5.41	47.54	-11.90	35.46
GS	119939	27349	152347	-7.25	48.58	-8.60	44.53
mi-SC	122305	152323	285394	-3.40	49.60	-11.79	35.82
m-SCS	109748	127363	244385	1.58	64.78	-11.06	38.48
L2ESA	140521	0	140521	3.98	80.60	0	0

An elevation map of the scatterers obtained from the CryoSat L2 processor of SARIn data from 2010 to 2015, using the Multi-Threshold Retracker, is displayed in Figure 4.

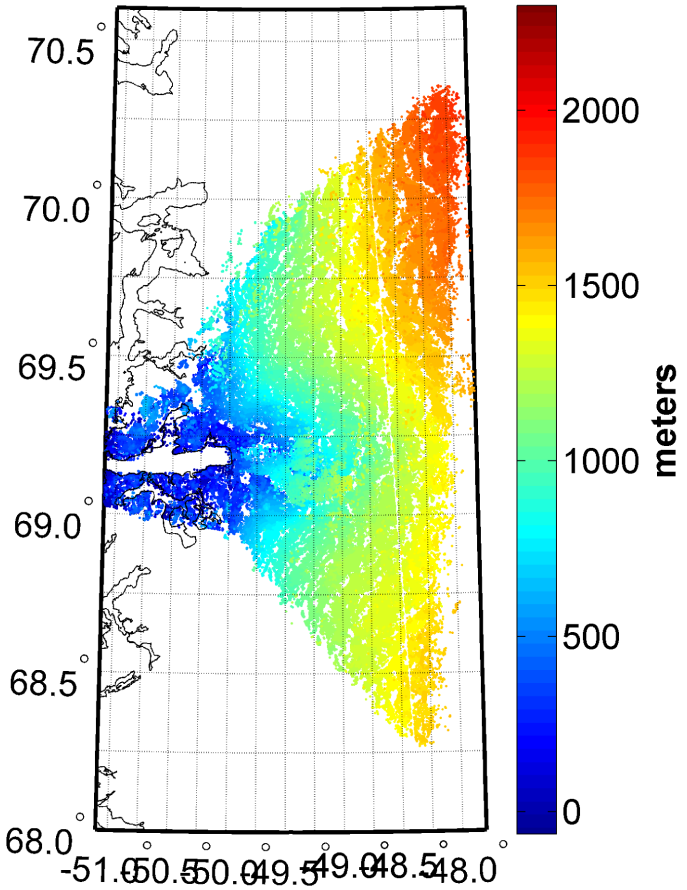

Figure 28: The map represents elevation of the Jakobshavn Isbræ with respect to the WGS 84 ellipsoid from CryoSat altimeter measurements from 2010 to 2015 using the Multi-Threshold Retracker

Figure 29 — 36 show the histograms of the elevation difference with the ICESat DEM for all retrackers implemented in the study.

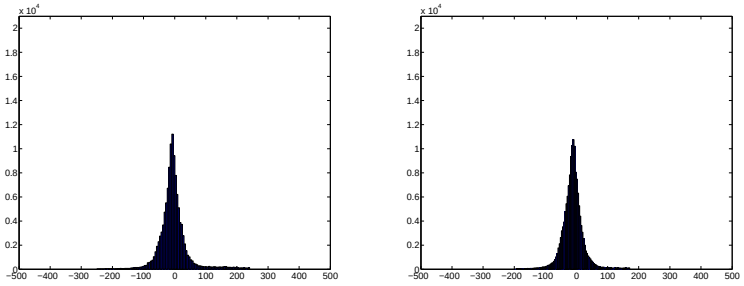

(a) POCA (b) non-POCA

Figure 29: Histogram of differences in meters between elevations obtained using the Multi-Threshold retracker and the ICESat DEM

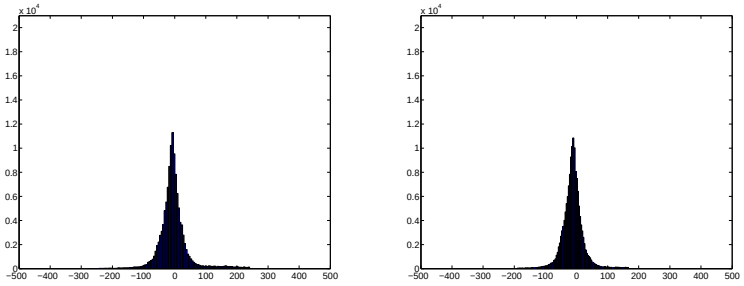

(a) POCA (b) non-POCA

Figure 30: Histogram of differences in meters between elevations obtained using the Multi-OCOG retracker and the ICESat DEM

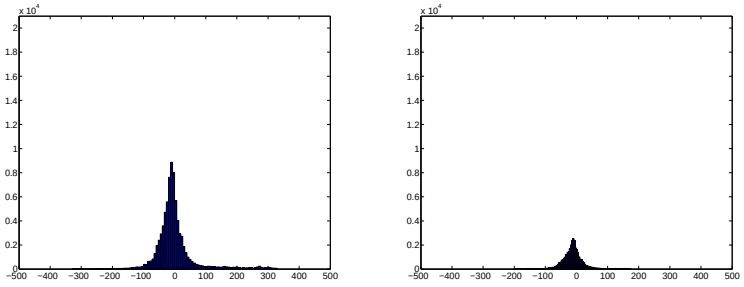

(a) POCA (b) non-POCA

Figure 31: Histogram of differences in meters between elevations obtained using the Beta retracker and the ICESat DEM

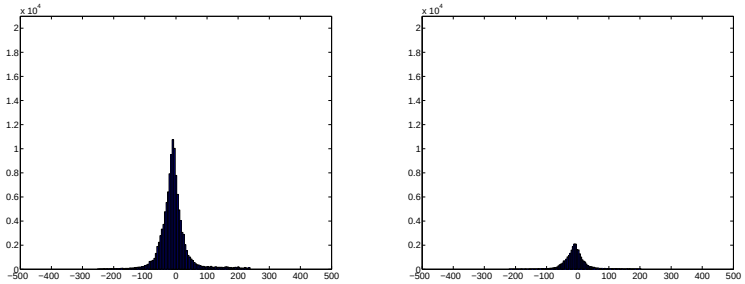

(a) POCA (b) non-POCA

Figure 32: Histogram of differences in meters between elevations obtained using the Gauss retracker and the ICESat DEM

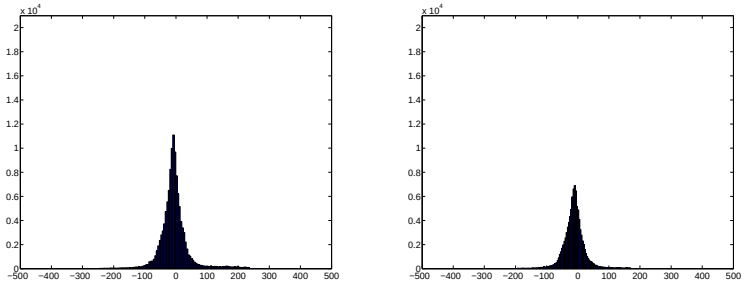

(a) POCA (b) non-POCA

Figure 33: Histogram of differences in meters between elevations obtained using the Multi-Gauss Threshold retracker and the ICESat DEM

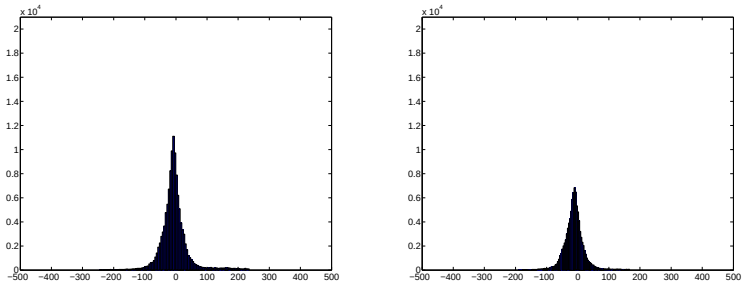

(a) POCA (b) non-POCA

Figure 34: Histogram of differences in meters between elevations obtained using the Multi-Gauss OCOG retracker and the ICESat DEM

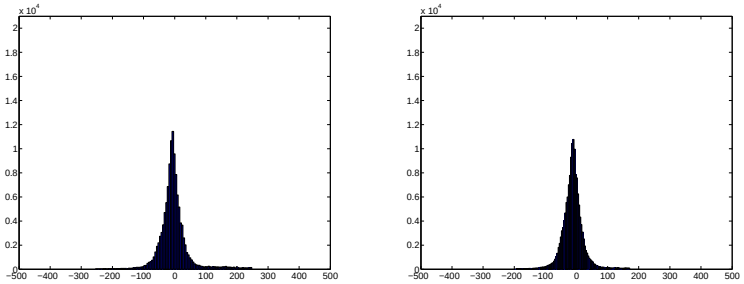

(a) POCA (b) non-POCA

Figure 35: Histogram of differences in meters between elevations obtained using the Multi-Simplified CryoSat retracker and the ICESat DEM

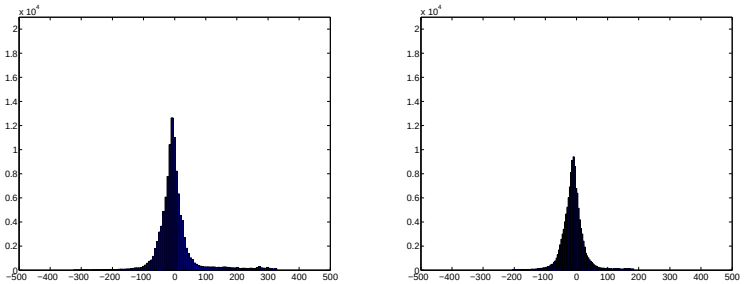

(a) POCA (b) non-POCA

Figure 36: Histogram of differences in meters between elevations obtained using the Multi-Simplified CryoSat II retracker and the ICESat DEM

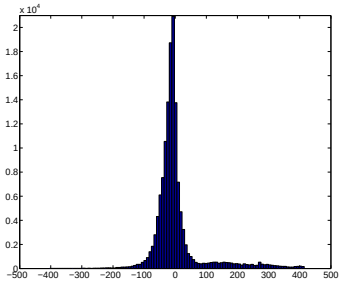

Figure 37: Histogram of differences in meters between elevations obtained using the ESA level 2 Processor and the ICESat DEM

4.2.3.1 *Discussion of elevation results from different retrackers*

Some important observations that are made in comparison to ESA's CryoSat level 2 data products are listed and discussed below:

1. **The total number of elevations from the multiple peak retrackers developed in this project is significantly larger than those from the CryoSat ESA level 2 data.**

   Our multiple peak retracking and interferometric processing approach provide more than one elevation estimate per waveform while the CryoSat level 2 processor developed by ESA only provides a single elevation estimate per waveform. The number of elevation estimates from the Multi-Threshold, Multi-COG and Multi-Simplified CryoSat retrackers are two times larger than the number of elevation estimates from the CryoSat ESA level 2 products.

2. **For each retracker, the number of elevations computed is less than the number of retracked peaks in a waveform.**

   It is possible that a retracker provides results that cannot be processed by the brute force interferometric processing algorithm. In such cases, our algorithm rejects that retracked peak from the waveform and no elevation is computed for that retracked peak.

3. **The level 2 ESA Products provide significantly larger number of CryoSat POCA elevations than our subwaveform retrackers.**

   This is because of two reasons:

   i) The number of CryoSat data files found within the same polygon described in Figure 25 for the CryoSat level 2 ESA Products was more than the number of CryoSat level 1b data files found within the same polygon. It is unsure why this is so. Maybe the application designed in this project for downloading large amounts of CryoSat data contains a code bug.

   ii) The methods implemented in this study discards noisy waveforms before retracking and computing elevations, whereas CryoSat level 2 products provide elevation estimates obtained from these noisy waveforms.

4. **The differences between the elevations computed from our retrackers and the ICESat DEM elevations do have a significantly lower standard deviation in comparison to the same from the CryoSat ESA level 2 Products.**

   The reduction can be almost 40%. From a comparison of Figures and , we conclude that the drop is likely caused by the fact that we have much less elevations in coastal regions close to the glacier tongue. This is because the topographical variations are larger, and the received waveforms contain more noise. Our

designed retrackers do not compute any elevations for these waveforms.

5. **The standard deviation of the difference between the non-POCA elevations computed from the multiple peak retrackers and the elevations from the ICESat DEM from DiMarzio *et al.* (2007) is lower than the same for the POCA elevations. However, the POCA elevation estimates from the multiple peak retrackers have a lower mean difference to the ICESat DEM elevations, in comparison to the non-POCA elevation estimates, except the Gauss retracker.**

   A possible explanation for the Gauss retracker behaving inconsistently with other implemented multiple peak retrackers is:

   i) The shapes of the POCA and the non-POCA subwaveforms are different. If a waveform contains multiple specular peaks within the receiving time window, the shapes of the subwaveforms are similar. If the waveform is non-specular and the subwaveforms are close to each other, the shape of the leading edge of the POCA subwaveform is different from the shape of the leading edge of the non-POCA subwaveform.

   ii) Retrackers like the Beta, Multi-Simplified CryoSat, and Multi-Simplified CryoSat II retrackers require information of the shape of the subwaveform for locating the leading edge. If the shapes of the subwaveforms of the POCA and non-POCA are not similar, the relative positions of the retracked bins on the leading edges with respect to the subwaveform maxima will be different.

   iii) Retrackers like the Multi-Threshold, Multi-OCOG, Multi-Gauss Threshold and Multi-Gauss OCOG rely on the shape of the leading edges for locating a retracker bin for the subwaveform. If the leading edge shapes of the POCA and the non-POCA subwaveforms are not similar, the relative position of the retracked bins on the leading edges with respect to the subwaveform maxima will be different.

   iv) The Gauss retracker is the only retracker in the 9 different retrackers shown in Table 3 that is symmetrical; the leading edge and the trailing edge of the subwaveform by the fit parameters a_n, b_n and c_n have the same slope magnitude. This symmetry results in a consistent performance of the Gauss retracker between POCA and non-POCA subwaveforms.

6. **The Multi-Simplified CryoSat II and the Beta retrackers have the smallest μ_{POCA}**

Looking at the histograms of the Multi-Simplified CryoSat II and the Beta retrackers in Figure 36 and Figure 31 respectively, there appear to be large positive differences between the elevations computed from the retrackers and the ICESat DEM along with a dominant negative difference distribution. This is not observed in other retrackers (Figures 29, 30, 32, 33, 34, 35). Because of this, the mean difference shifts towards the positive side. The same is observed for the level 2 ESA data products, that contain large positive differences with the ICESat DEM.

In Figure 38, a map of the elevation differences between computed elevations from the ESA Processor and the ICESat DEM, and computed elevation from our implementation of the Multi-Simplified CryoSat II Retracker and the ICESat DEM is provided.

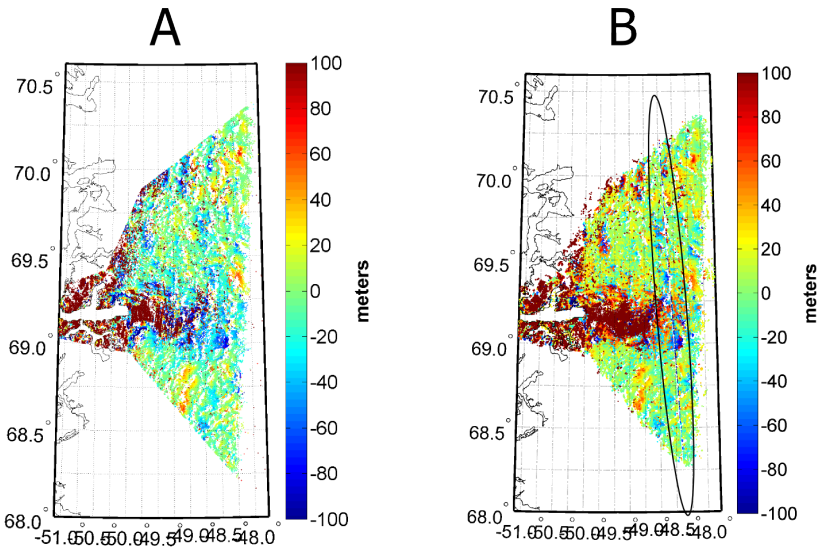

Figure 38: Figure A represents a map of difference between the elevations from the CryoSat ESA level 2 Products and the ICESat DEM elevations at those points. Figure B represents the same for elevations computed from the Multi-Simplified CryoSat II retracker.

From the figure, the following observations and conclusions are drawn:

1. **In both cases, there appear to be areas where the computed elevations differ from the ICESat DEM by more than 100 m.**

   Looking at Figure 38, we observe that large offsets are prevalent in regions on high surface variability. These regions are the glacial lake, the rocky terrain and multiple areas all over the basin that may have large spatial variations over a couple of meters. A reason why this could be so is that the uncertainty of the DEM in these regions could be very high, and also the level

2 results in these regions could be erroneous. This in an indication that spaceborne radar altimetry is insufficient for mapping areas with very high variability.

2. **There seems to be an artifact due to large negative departure from the ICESat DEM from a single satellite track in Figure B. This is not observed in Figure A.**

   The cause of this artifact is unknown. It appears that this is specific to a single satellite track.

3. **The level 2 ESA elevation differences from the ICESat DEM show a dominant negative spatial trend, even though Table 3 suggests a positive mean difference.**

   Looking at the histogram of these difference in Figure Figure 37, the level 2 ESA elevations contain very large positive mean differences in the order of 100 m that cause the mean difference to the ICESat DEM to shift from the negative to the positive side.

4.3 ELEVATION CHANGE RESULTS FROM THE DIFFERENT RETRACKERS

The results from the different retrackers were used to estimate the linear elevation change trends over the specified basin polygon using the methodology described in Chapter 3.4. Table 4 provides the linear elevation change trend statistics of elevations computed from the results of different designed retrackers described in Chapter 3. These numbers are obtained after a coarse outlier detection to remove unrealistic elevation change results (absolute values greater than 50 meters/year). This outlier detection is done by checking whether each elevation change value at a specific location is within 2 times the standard deviation around the mean of all points within a certain degree range (0.0899° in our case, from Matlab's `deg2km(10)`) from its position. If this is not the case, the elevation change point is removed from the data. Second, a final Grubb's test was applied to remove remaining outliers. Figures 40 and 42 show maps of the linear elevation change trend estimates computed from our level 2 CryoSat elevations between 2010 to 2015. Figure 39 represents linear elevation change trends computed from CryoSat ESA level 2 data products between 2010 to 2015. The histograms shown in Figure 42 represent the distribution of the elevation change results from different algorithms used in this study.

Table 4: Statistics of the linear elevation change trend estimates from data acquired over July 2010 to March 2015 using the elevation estimates from different CryoSat level 2 Processors downloaded or implemented in this study. The parameters are: i) number of points n_p, ii) the mean of the elevation change over the specified polygon in meters/year $\mu_{\triangle H}$, iii) the standard deviation of the elevation change computed in meters/year $\sigma_{\triangle H}$, iv) the maximum negative elevation change in meters/year $\min_{\triangle H}$, v) the maximum positive elevation change in meters/year $\max_{\triangle H}$, vi) the % of the total number of positive elevation change points $\%_+$, and vii) The total number of points within the bounding box in Figure 39. n_{bb}

Name	n_p	$\mu_{\triangle H}$	$\sigma_{\triangle H}$	$\min_{\triangle H}$	$\max_{\triangle H}$	$\%_+$	n_{bb}
m-T	135952	-1.68	2.26	-13.19	9.82	11.03	36030
m-OCOG	133964	-1.68	2.25	-13.10	9.73	11.05	35462
Beta	19782	-1.34	2.07	-11.04	8.37	16.44	3601
m-GT	88699	-1.61	2.19	-12.56	9.33	11.48	22003
m-GOCOG	88969	-1.64	2.12	-12.23	8.93	10.53	22165
GS	37285	-1.46	2.08	-11.48	8.57	13.15	8137
m-SC	133576	-1.67	2.29	-13.28	9.95	11.36	35141
m-SCS	95054	-1.64	2.37	-13.54	10.27	12.64	24580
L2ESA	26614	-1.27	2.71	-14.20	11.65	17.91	5471

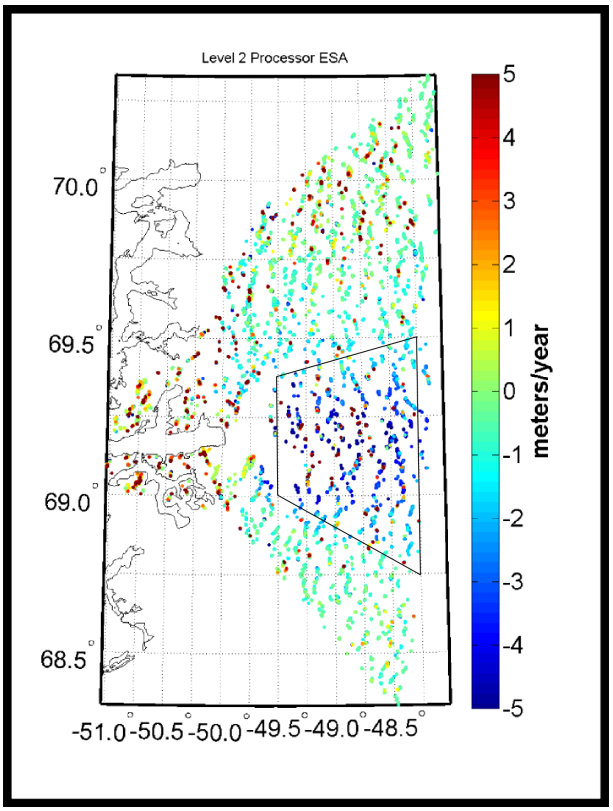

Figure 39: CryoSat ESA level 2 processor elevation changes between July 2010 to March 2015.

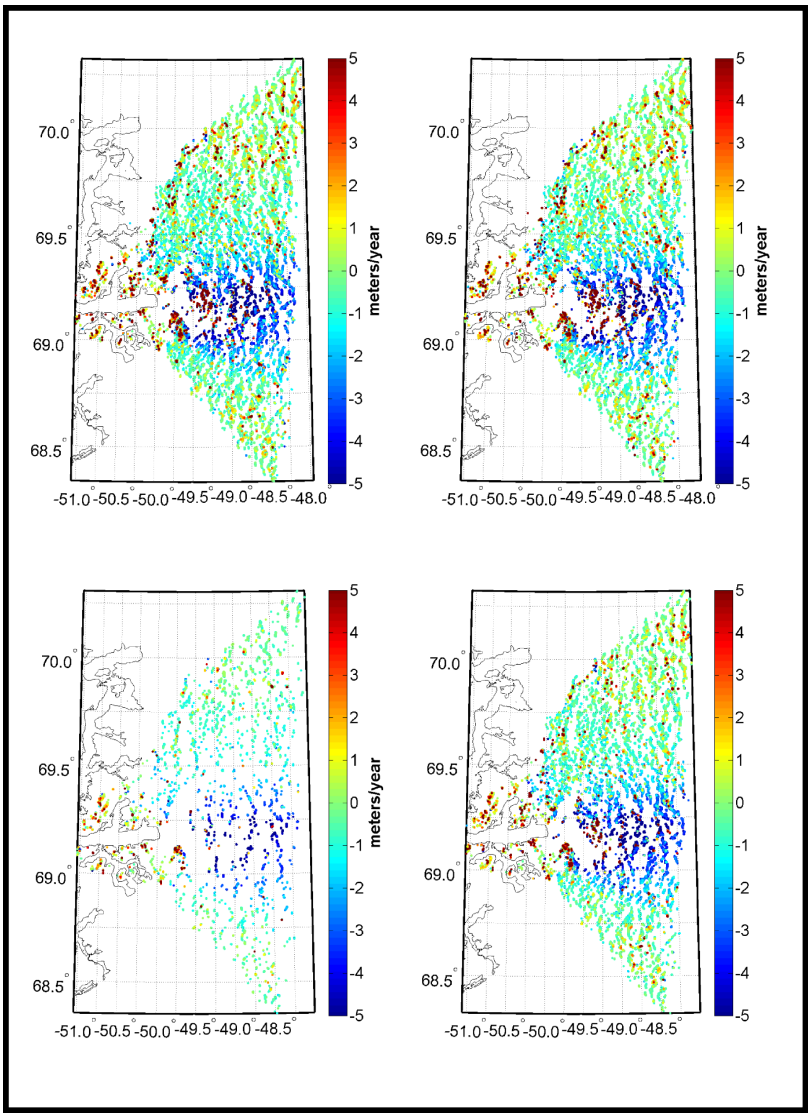

Figure 40: Linear inter-annual elevation trends between 2010 and 2015 for elevations computed from: i) the Multi-Threshold retracker (top-left), ii) the Multi-OCOG retracker (top-right), iii) the Beta retracker (bottom-left), and iv) The Gauss Threshold retracker (bottom-right).

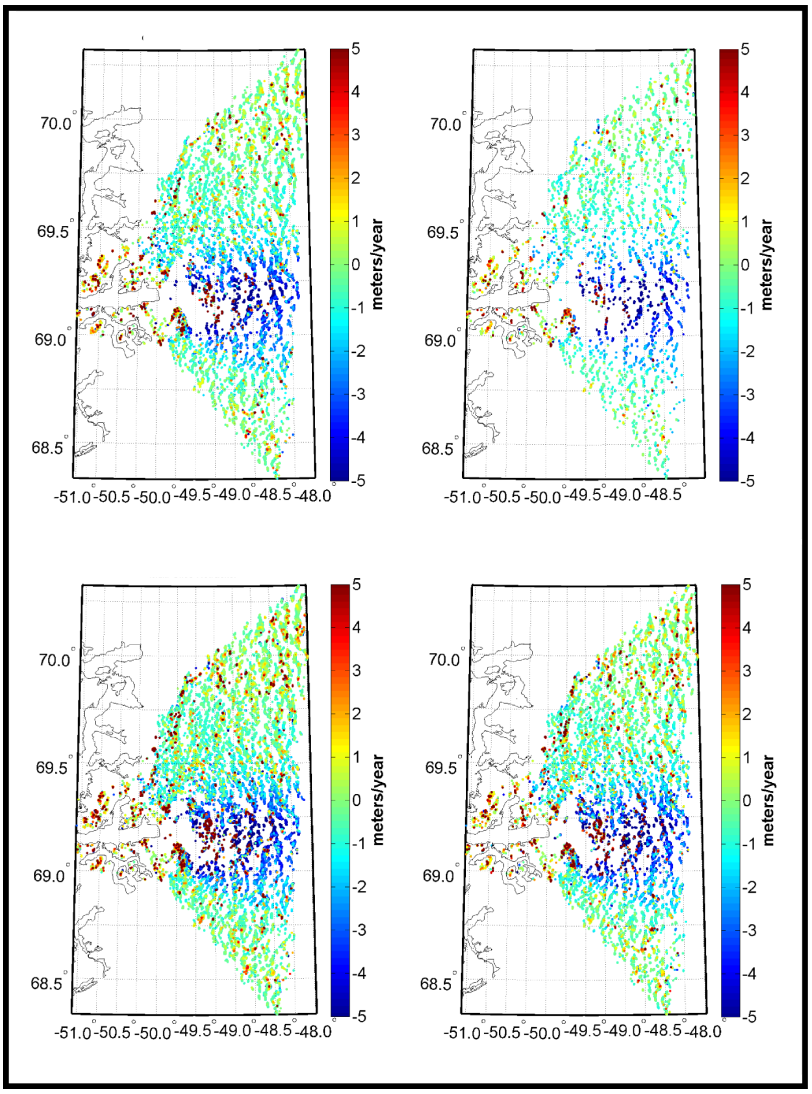

Figure 41: Linear inter-annual elevation trends between 2010 and 2015 for elevations computed from: i) the Multi-Gauss OCOG retracker (top-left), ii) the Gauss retracker (top-right), iii) the Multi-Simplified CryoSat retracker (bottom-left), and iv) The Multi-Simplified CryoSat II retracker (bottom-right).

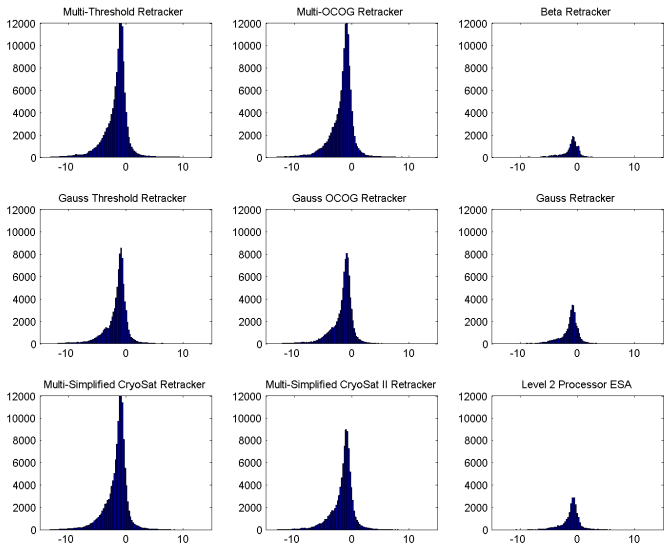

Figure 42: Histograms of the linear elevation change trends computed using the various retrackers.

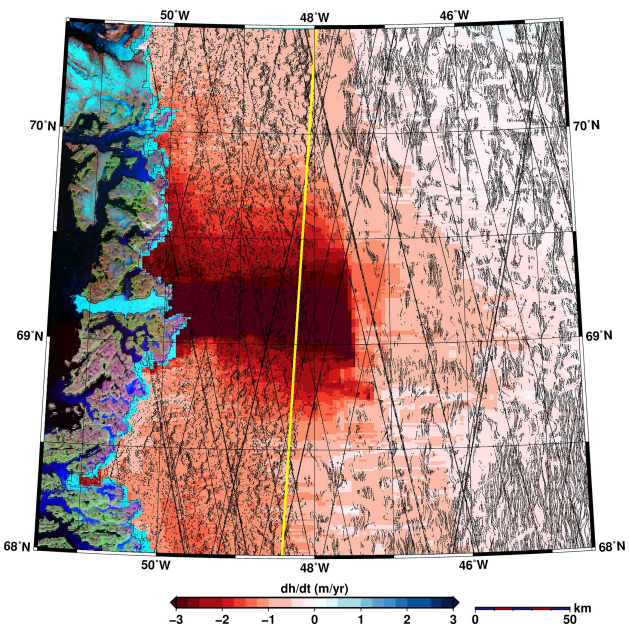

Figure 43: The map, adopted from Helm *et al.* (2014), shows the spatial variation of the elevation change observed from 2011 to 2014 in the Jakobshavn basin. The yellow line represents the boundary of the SARIn data.

4.3.1 *Discussion of elevation change results*

The following observations are drawn from the elevation change results presented:

1. **The elevations from the subwaveform approach provide a larger number of linear elevation change trend estimates in comparison to the same from ESA level 2 products, and hence a better spatial sampling of the observed signal.**

   The reason is two fold:

   i) The subwaveform approach provides large number of scatterers at which elevation trends can be computed.

   ii) Scatterers at much farther off-nadir angles fall within the neighbourhood of other scatterers during elevation change computation. Hence, less points are rejected that do not meet the criterion outlined in section 3.4.

   We observe a clear spatial trend of negative elevation changes that is similar to the results obtained by Helm *et al.* (2014) for the Jakobshavn basin. While Helm *et al.* (2014) observed a much lower elevation change (Figure 43) that does not exceed -3 m/yr between 2011 and 2014 (according to them, the spatial averaging technique they implemented influenced this result), the spatial

signal was clear. This kind of signal is also observed in Figure 26 by Thomas *et al.* (2009).

The parameter $n_{polygon}$ from Table 4 provides the total number of elevation trend estimates within the polygon described in Figure 39. The polygon is a rough bounding box of the observed spatial elevation trend distribution. The number of elevation trend estimates from the subwaveform approach within this polygon is much larger than the number of elevation trend estimates within the same polygon computed from the elevations of ESA level 2 data.

2. **Some points show a strong positive linear elevation change trend inside the polygon outlined in Figure 39.**

   Possible explanations for this can be:

   i) An actual positive elevation change due to flow of ice. This is because if at a specific time the radar altimeter computes elevation for a point on the glacier basin, the same geographic location's topography can change due to the flow of ice.

   ii) Incorrect parameterization of the topography. If the functional model is not correct, the topographical signal will leak into the linear trend estimates. This is observed in areas showing strong topographical variability.

   Table 4 provides the parameter $n_{positive}$, which is the percentage of positive inter-annual elevation trend estimates. The elevation estimates from the ESA level 2 processor, the Beta retracker and the Gauss retracker contain more number of positive elevation trends than the results from the subwaveform approach. These three algorithms also provide the smallest number of elevation estimates.

3. **The mean elevation trend over the Jakobshavn polygon from the Beta retracker, the Gauss retracker and the ESA level 2 products is less negative and inconsistent with the same from other retrackers in Table 4.**

   The histograms of the elevation trends from the Beta retracker, the Gauss retracker and the level 2 products from ESA are very different from the histograms of the elevation trends from the other retrackers. From Figure 42, we observe that the number of negative elevation trend estimates from the subwaveform retrackers decreases gradually with increasing negative elevation trends. This behaviour is not observed from the histograms of the elevation trend estimates from the beta retracker and the ESA level 2 products. Because of this, the mean of the elevation trend estimates do not have a larger negative value.

4. **The standard deviations of the linear elevation trend estimates from the algorithms that retrack multiple peaks is lower than the same from CryoSat ESA level 2 products.**

   This suggests that the linear elevation trend estimates using the multiple scatterer retrackers are more consistent than the linear elevation trend estimates from a single scatterer retracking algorithm.

4.4 CONCLUSION

From the analysis of the results obtained using our subwaveform retracking approach, we observe a much larger number of elevations and linear elevation change trend estimates, in comparison to the same from the CryoSat level 2 data products from ESA. From the discussion of results in this chapter, we conclude the following:

1. A multiple scatterer retracking approach for CryoSat SARIn data provides a better picture of the Jakobshavn drainage basin than a single scatterer retracking approach based on the same data.

2. A multiple scatterer retracking approach provides a larger number linear elevation change trend estimates that are also more consistent in comparison to the linear elevation change trends estimated from the data products of ESA, using the same elevation change computation approach.

3. The subwaveform approach works best with robust retracking algorithms like the Threshold and the OCOG retrackers, and is also beneficial in providing initial conditions for retrackers that require an analytical model to retrack multiple peaks. This was observed with our implementation of the Multi-Simplified CryoSat retracker. However, the subwaveform approach does not perform as well when an analytical model is fit through each of the subwaveforms. The Multi-Simplified CryoSat retracker did not perform as consistently as the Multi-Threshold, the Multi-OCOG and the Multi-Simplified CryoSat retrackers, even though it worked with the same number of waveform peaks.

The next chapter finalises this thesis by providing answers to the research questions proposed in Chapter 1, and provides recommendations for future work.

5 CONCLUSIONS AND RECOMMENDATIONS

This chapter answers the research questions discussed in Chapter 1, and provides recommendations for future research.

5.1 SUBWAVEFORM RETRACKING METHOD

The first research question was: *Can a retracker process CryoSat SARIn waveforms to retrieve multiple elevation estimates per waveform?* This question has been addressed in Chapter 3.

5.1.1 *Conclusions*

In this project the shape of the received SARIn waveform was studied. It was observed that multiple individual peaks in a waveform shared similar characteristics; i) a leading edge, ii) a peak, and iii) a trailing edge. A method was designed to exploit this geometry by splitting the full waveform into multiple subwaveforms. After that, we applied existing and newly developed retrackers to each subwaveform in order to retrack multiple peaks. The retrackers used were the Threshold retracker from Davis (1997), the OCOG retracker from Wingham *et al.* (1986), the Simplified CryoSat retracker from Giles *et al.* (2007), and some Gaussian-based retrackers. From these four retrackers, six different subwaveform-modified versions and a separate symmetric Gaussian retracker were obtained. These retrackers were tested together with the beta retracker from Martin *et al.* (1983), which was not modified for this study.

From the results in Chapter 4, we conclude that the designed multiple scatterer retrackers designed are able to retrack scatterers that lie beyond the POCA in the range window of the CryoSat SIRAL altimeter. From a compatibility point of view, it was observed that the robust numerical retrackers greatly benefited from the subwaveform approach, whereas the subwaveform functional retrackers did not provide as many retracked peaks. It was also observed that the subwaveform approach could be used to provide initial conditions to multi-peak retrackers that implemented analytical models. This was observed in the case of the Multi-Simplified CryoSat II retracker, which located the leading edges of multiple peaks in a waveform by fitting functional models to the subwaveforms. Even though the retracker was provided with the same number of subwaveforms as the Multi-Threshold, the Multi-OCOG and the Multi-Simplified CryoSat

retracker, it still did not produce the same number of retracked peaks, while the other three did.

We conclude that it is possible to retrack multiple peaks in a CryoSat SARIn waveform using the subwaveform approach.

5.1.2 *Future Recommendations*

Three out of the eight retrackers implemented require a threshold value that defines the relative position of the leading edge bin of the waveform peak with respect to the peak power. In our study, this retracker threshold was set to 80% of the total maximum received power in the waveform. We note that it is important to choose an *defendable* threshold chosen based on some criteria. For example, a threshold of 40% of the first maxima in the received waveform was implemented by Helm *et al.* to account for the penetration of radar signal into the ice. In ice sheet retracking, often the retracker comes across specular or non-specular waveforms. In both cases it is beneficial to choose an optimal retracking threshold. We recommend to study which retracker threshold best explains the location of the scatterer in the range window of the CryoSat altimeter.

5.2 PERFORMANCE OF THE ELEVATION ESTIMATES COMPUTED FROM THE SUBWAVEFORM APPROACH

The second research question was: *How does the proposed retracking scheme compare to the available Level 2 CryoSat SARIn data products from ESA?* This question has been discussed in Chapter 4. This section also answers the third research question proposed: *What is the impact of applying this developed technique for studying ice sheet elevation changes?* This has also been discussed in Chapter 4.

5.2.1 *Conclusions*

The elevation estimates obtained after implementing the proposed retracking scheme over the Jakobshavn Isbræ were compared to the elevation estimates from CryoSat ESA Level 2 products over the same area. The following is a summary of the results:

i) The total number of elevation estimates from the subwaveform retrackers (except the Multi-Simplified CryoSat II retracker) was two times larger than the total number of elevation estimates from the CryoSat ESA Level 2 data products.

ii) The absolute mean difference between the elevation estimates from the ESA Level 2 products and the ICESat DEM provided by DiMarzio *et al.* (2007) was much lower than the absolute

mean difference between the elevation estimates from the multiple scatterer retrackers developed in this project and the elevations from the ICESat DEM. This was explained by the tail of the histogram of the differences. The ESA level 2 data have a longer right hand side tail with difference upto 400 meters.

iii) The standard deviation of the differences in the case of the ESA level 2 data was significantly larger. This was because the ESA level 2 products provided elevation data over areas that showed strong topographical variability, whereas our method did not. These elevations had large differences from the DEM that contributed the large standard deviation number.

To study ice sheet elevation changes, the spatio-temporal elevation change trend estimation technique from Wouters *et al.* (2015) was adopted. The elevation change trends estimated between 2010 and 2015 with the multiple peak retrackers were compared to the same from the elevations of ESA Level 2 products over the same area. The multiple peak retrackers designed in this study provided more elevation change estimates with a lower standard deviation than the same from the ESA Level 2 products.

In conclusion, the subwaveform approach has a positive impact in elevation change studies as it improves the spatial sampling of the observed signals.

5.2.2 *Future Recommendations/Suggested Improvements*

To improve elevation change estimates, it would be beneficial to improve the estimation of the functional model that accounts for the topography. A possible alternative could be to implement the method described by Helm *et al.* (2014), who removed the effect of topography by generating a DEM from the elevation estimates and subtracted interpolated elevation values at the position of each elevation estimate.

5.3 STATUS OF THE RESEARCH PROJECT

This section concludes this research document by discussing whether the proposed research objective was achieved, and describes future possible research that could benefit from the developed method in this research project.

5.3.1 *Did we achieve the research objective?*

After answering the research questions, this section evaluates the status of the project with respect to achieving the primary research objective discussed in Chapter 1: *Design an algorithm that utilizes the entire return echo data of CryoSat to study elevation change over ice sheets.*

We successfully increased the total number of elevation estimates which lead to an increase in the total number of elevation change estimates in comparison to Level 2 processors that do not implement our subwaveform approach. Hence, we indeed utilized the entire return echo data of CryoSat.

5.3.2 *Future possible research in line with this research*

We propose the following research topics:

1. Computation of coastal ice sheet mass variations using CryoSat data and multiple peak retracking algorithms.
2. Computation of glacier basin volume changes using CryoSat data and multiple peak retracking algorithms.
3. Adjusting the multiple peak retracking algorithms to accommodate the new Baseline C Level 1b data.
4. DEM generation using multiple scatterer retracker results.
5. Estimation of intra-annual elevation changes.
6. Application of the designed method in this project over the entire coastal zone of Greenland.
7. Comparison of the CryoSat subwaveform estimates to other atimeters, like the NASA ATM, or the ICEBridge missions, ICESat, etc.

BIBLIOGRAPHY

A.C. Brenner, R.A. Bindschlader, R.H. Thomas H.J. Zwally. 1983. Slope-Induced Errors in Radar Altimetry Over Continental Ice Sheets. *Journal of Geophysical Research*.

Bamber, J. L. 1994. Ice sheet altimeter processing scheme. *International Journal of Remote Sensing*.

Bliss, Andy. 2011 (December). *Map coordinates in Polar Stereographic system to Geodetic Latitude and Longitude*.

Brenner, Anita C., DiMarzio, John P., & Zwally, H. Jay. 2007. Precision and accuracy of satellite radar and laser altimeter data over the continental ice sheets. *IEEE Transactions on Geoscience and Remote Sensing*.

Brown, Gary S. 1977. The Average Impulse Response of a Rough Surface and Its Applications. *IEEE Transactions on Antennas and Propagation*.

Cole, S., McCarthy L. 2015. *NASA, NOAA Find 2014 Warmest Year in Modern Record*.

Davis, C. H. 1993. A surface and volume scattering retracking algortihm for ice sheet satellite altimetry. *IEEE Transactions on Geoscience and Remote Sensing*, **31**(4), 811–818.

Davis, Curt H. 1997. A Robust Threshold Retracking Algorithm for Measuring Ice-Sheet Surface Elevation Change from Satellite Radar Altimeters. *IEEE Transactions on Geoscience and Remote Sensing*.

Deng, X., & Featherstone, W. E. 2006. a coastal retracking system for satellite radar altimeter waveform : Application to ERS-2 around Australia. *Journal of Geophysical Research*, **111**.

DiMarzio, J., Brenner, A., Schutz, R., Shuman, C. A., & Zwally, H. J. 2007. *GLAS/ICESat 1 km laser altimetry digital elevation model of Greenland*.

Echelmeyer, K., Clarke, T. S., & Harrison, W. D. 1993. Surficial Glaciology of Jakobshavns Isbr *Journal of Glaciology*, **38**(128).

ESA. 2014 (February). *CryoSat Data Quality Status Summary: http://eopi.asi.it/documents/10174/129120/CryoSat_IPF_anomalies, Accessed: July 14, 2015*.

ESA, & Laboratory, Mullard Space Science. CryoSat Product Handbook, http://emits.sso.esa.int/emits-doc/ESRIN/7158/CryoSat-PHB-17apr2012.pdf.

F. Remy, P. Mazzega, S. Houry C. Brossier, & Minister, J.F. 1989. Mapping of the topography of continental ice by inversion of satellite-altimeter data. *Journal of Glaciology*.

Galin, Natalia, Wingham, Duncan J., Cullen, Robert, Frnari, Marco, Smith, Walkter H. F., & Abdalla, Saleh. 2013. Calibration of the CryoSat-2 Interferometer and Measurement of Across-Track Ocean Slope. *IEEE Transactions on Geoscience and Remote Sensing*, **51**(1).

Giles, K. A., Laxon, S. W., Wingham, D. J., Wallis, D. W., Krabill, W. B., Leuschen, C. J., McAdoo, D., Manizade, S. S., & Raney, R. K. 2007. Combined airborne laser and radar altimeter measurements over the Fram Strait in May 2002. *Remote Sensing of Environment*, **111**(2-3), 182–194.

Gray, L., Burgess, D., Copland, L., Cullen, R., Galin, N., Hawley, R., & Helm, V. 2013. Interferometric swath processing of Cryosat data for glacial ice topography. *The Cryosphere*.

Grubbs, Frank E. 1969. Procedures for detecting outlying observations in samples. *Technometrics*, **11**(1), 1–21.

Helm, V., Humbert, A., & Miller, H. 2014. Elevation and elevation change of Greenland and Antarctica derived from CryoSat-2. *The Cryosphere*.

Holland, David M., Thomas, Robert H., de Young, Brad, Ribergaard, Mads H., & Lyberth, Bjarne. 2008. Acceleration of Jakobshavn Isbræ triggered by warm subsurface ocean waters. *Nature Geoscience*, **1**(September), 659–664.

Hua, Aixue, Meehla, Gerald A., Hanb, Weiqing, & Yinc, Jianjun. 2011. Effect of the potential melting of the Greenland Ice Sheet on the Meridional Overturning Circulation and global climate in the future. *Deep Sea Research Part II: Topical Studies in Oceanography*, **58**(September), 1914–1926.

Hurkmans, R. T. W. L., Bamber, J. L., & Griggs, J. A. 2012a. Importance of slope-induced error correction in volume change estimates from radar altimetry. *The Cryosphere*.

Hurkmans, R. T. W. L., Bamber, J. L., Sørensen, L. S., Joughin, I. R., Davis, C. H., & Krabill, W. B. 2012b. Spatiotemporal interpolation of elevation changes derived from satellite altimetry for Jakobshavn Isbrae, Greenland. *Journal of Geophysical Research*, **117**(September).

Jensen, J. R. 1995. Design and performance analysis of a phase-monopulse radar altimeter for continental ice sheet monitoring. *Proceedings, IEE International Geoscience and Remote Sensing Symposium IGARSS'95. Florence, Italy*, 865–867.

Johannessen, Ola M., Khvorostovsky, Kirill, Miles, Martin W., & Bobylev, Leonid P. 2005. Recent Ice-Sheet Growth in the Interior of Greenland. *Science*.

Joughin, Ian, Abdalati, Waleed, & Fahnestock, Mark. 2004. Large fluctuations in speed on Greenland's Jakobshavn Isbraw glacier. *Nature*, **432**(December).

Luckman, Adrian, & Murray, Tavi. 2005. Seasonal variation in velocity before the retreat of Jakobshavn Isbræ˙ *Geophysical Research Letters*, **32**.

Martin, Thomas V., Zwally, H. Jay, Brenner, Anita C., & Bindschadler, Robert A. 1983. Analysis and Retracking of Continental Ice Sheet Radar Altimeter Waveforms. *Journal of Geophysical Research*.

McMillan, Malcolm, Corr, Hugh, Shepherd, Andrew, Ridout, Andrew, Laxon, Seymour, & Cullen, Robert. 2013. Three-dimensional mapping by CryoSat-2 of subglacial volume changes. *Geophysical Research Letters*, **40**(August), 4231–4327.

Messerli, A., Karlsson, N. B., & Grinsted, A. 2014. Brief Communication: 2014 velocity and flux for five major Greenland outlet glaciers using ImGRAFT and Landsat-8. *The Cryosphere Discussions*, **8**(6), 6235–6250.

Motyka, Roman J., Truffer, Martin, Fahnestock, Mark, Mortensen, John, ren Rysgaard, Sø, & Howat, Ian. 2011. Submarine melting of the 1985 Jakobshavn IsbrÃę floating tongue and the triggering of the current retreat. *Journal of Geophysical Research*, **116**.

Nick, Faezeh M., Vieli, Andreas, Andersen, Morten Langer, Joughin, Ian, Payne, Antony, Edwards, Tamsin L., Pattyn, Frank, & van de Wal, Roderik S. W. 2013. Future sea-level rise from GreenlandâĂŹs main outlet glaciers in a warming climate. *Nature*.

Raney, R. Keith. 1998. The Delay-Doppler radar altimeter. *IEEE Transactions on Geoscience and Remote Sensing*.

Remy, Frederique, & Parouty, Soazig. 2009. Antarctic Ice Sheet and Radar Altimetry: A Review. *Remote Sensing*.

Ridley, J. K., & Partington, K. C. 1988. A mode of satellite radar altimeter return from ice sheets. *International Journal of Remote Sensing*, **9**.

Shoelson, Brett. 2011 (March). *An implementation of the Grubb's test: http://in.mathworks.com/matlabcentral/fileexchange/3961-deleteoutliers, Accessed: May, 2015*.

Stenseng, Lars. 2011 (September). *Polar Remote Sensing by CryoSat-type Radar Altimetry*. Ph.D. thesis, Danmarks Tekniske Universitet.

Thomas, R., Frederick, E., Krabill, W., Manizade, S., & Martin, C. 2009. Recent changes on Greenland outlet glaciers. *Journal of Glaciology*, **55**(189).

Wingham, D. J., Francis, C. R., Baker, S., Bouzinac, C., Brockley, D., Cullen, R., de Chateau-Thierry, P., Laxon, S. W., Mallow, U., Mavrocordatos, C., Phalippou, L., Ratier, G., Rey, L., Rostan, F., Viau, P., & Wallis, D. W. 2006. CryoSat: A mission to determine the fluctuations in Earth's land and marine ice fields. *Advances in Space Research*.

Wingham, D.J. 1999. *CryoSat Science and Mission Requirements*.

Wingham, D.J., Rapley, C. G., & Griffiths, H. 1986. New Techniques in Satellite Tracking Systems. *In: Proceedings of IGARSS' 88 Symposium*.

Wouters, B., Martin-Espanol, A., Helm, V., Flament, T., van Wessem, J. M., Ligtenberg, S. R. M., van den Broeke, M. R., & Bamber, J. L. 2015. Dynamic thinning of glaciers on the Southern Antarctic Peninsula. *Science*, **348**(6237), 899–903.